GEORG-AUGUST-UNIVERSITÄT GÖTTINGEN

Fakultät für Physik

Bachelor's Thesis

Untergrundstudien in der Suche nach Zerfällen von schweren Higgs Bosonen in zwei Tau Leptonen produziert bei $\sqrt{s} = 13$ TeV pp-Kollisionen am ATLAS

Background studies in the search for heavy Higgs bosons decaying to two tau leptons in $\sqrt{s} = 13$ TeV pp-collisions at ATLAS

prepared by

Anne Gaa

from anne.gaa@stud.uni-goettingen.de

at the II. Physikalischen Institut

Thesis number:	II.Physik-UniGö-BSc-2020/08
Thesis period:	11th May 2020 until 27th August 2020
First referee:	Prof. Dr. Stan Lai
Second referee:	Prof. Dr. Arnulf Quadt

Abstract

In dieser Bachelorarbeit wird die mögliche Existenz schwerer Higgs Bosonen im $H/A \to \tau\tau$ Kanal des ATLAS Experiments untersucht bei $\sqrt{s} = 13$ TeV pp-Kollisionen mit einer integrierten Luminosität von 139 fb^{-1}. Fokus hierbei liegt auf dem hadronischen Zerfall der τ Leptonen, dessen wichtigster Hintergrund aus Multijets besteht. Dieser Multijet Hintergrund wird mit der fake factor Methode berechnet.
Konkretes Thema dieser Arbeit ist, eine mögliche Verbesserung der fake factor Methode zu untersuchen in Form einer zusätzlichen Unterscheidung in einer neuen Variable, der Pseudorapidität des subleading τ Leptons. Diese Untersuchung wird in den beiden derzeit von ATLAS verwendeten τ Lepton Identifikationsalgorithmen durchgeführt, der Boosted Decision Tree (BDT) ID und der Recurrent Neural Network (RNN) ID. Die Ergebnisse dieser Untersuchung werden vorgestellt und besprochen.

Abstract

In this bachelor the possible existence of heavy Higgs bosons is examined in the $H/A \to \tau\tau$ channel of the ATLAS experiment at $\sqrt{s} = 13$ TeV pp-collisions corresponding to an integrated luminosity of 139 fb^{-1}. The focus lies on the hadronically decaying τ leptons, whose most significant background consists of multijet events. This multijet background is estimated via the fake factor method.
The concrete subject of this thesis is the evaluation of a possible improvement to the fake factor method in the form of an introduction of an additional dependence in a second variable, the pseudorapidity of the subleading τ lepton. This evaluation is conducted in both τ lepton identification algorithms currently used by ATLAS, the Boosted Decision Tree (BDT) ID and the Recurrent Neural Network (RNN) ID. The results of this evaluation are presented and discussed.

Contents

1 Introduction **1**

2 The Standard Model and the BEH Mechanism **2**
2.1 Overview of the Standard Model 3
2.2 The BEH Mechanism 5
2.3 Shortcomings of the Standard Model 6

3 The Minimal Supersymmetric Standard Model **7**
3.1 Motivation for Supersymmetry 7
3.2 The Higgs Sector of the MSSM 8

4 The LHC and the ATLAS Detector **10**
4.1 The LHC Accelerator Chain 10
4.2 The ATLAS Detector 11
4.2.1 Inner Detector 12
4.2.2 Calorimetry 13
4.2.3 Muon Spectrometer 14
4.2.4 Trigger System 14

5 Search for the heavy neutral Higgs Boson in the $\tau_{had}\tau_{had}$ Final State **16**
5.1 Event Reconstruction and Selection 16
5.2 Background Estimation Methods 18
5.2.1 The Fake-Factor Method 18
5.3 Systematic Uncertainties in the $\tau_{had}\tau_{had}$ and $\tau_{lep}\tau_{had}$ channel 20
5.4 Results in the Search for the heavy neutral Higgs Boson at ATLAS 20

6 Improvements to the Fake-Factor Method **23**
6.1 BDT- and RNN-ID 23
6.2 Motivation and Implementation 2d-Binning Method 27
6.3 Results 33

7 Conclusion **36**

1 Introduction

The field of particle physics investigates the fundamental constituents of the universe. For this, it needs to be able to describe the elementary particles and the different ways they interact with each other. The Standard Model of particle physics [1, 2] is the most recent theory for these particles and their interactions, and provides good experimental predictions. But there are problems regarding the Standard Model, namely that it is incomplete. Several phenomena exist that cannot be explained by it. Hence, particle physicists search for physics beyond the Standard Model.

One instance of physics beyond the Standard Model would be the existence of heavy Higgs bosons. The search for such particles involves the reconstruction of possible decay products, for example from two τ leptons. In the analysis of these decay channels, there is always a large amount of background, so algorithms and selection criteria are established to isolate the signal from the different backgrounds.

This Bachelor thesis tries to improve the modelling of the multijet background estimate in the ATLAS analysis of the $H/A \to \tau\tau$ channel. The fake-factor method provides a robust modelling of the multijet contribution, which is an important background for the signal in this channel. A two-dimensional dependence of the fake-factor and its benefits to the modelling of the background estimate are analyzed. The analysis was conducted in both τ lepton identification algorithms currently used by ATLAS, the BDT- and RNN-ID. Motivation and implementation for this approach are presented and the resulting modelling of the multijet background estimate in various variables in comparison to the one-dimensional fake-factor approach is discussed.

2 The Standard Model and the BEH Mechanism

The Standard Model (SM) [1, 2] provides the theoretical framework for particle physics. It describes and categorizes elementary particles and their interactions. These interactions are divided into three of the known forces in the universe: the electromagnetic, the weak and the strong interaction, with gravitation as the fourth force not being part of the SM. This needs to be corrected for a complete theory of the fundamental interactions, but until now, the SM is a consistent theory for the three forces it covers and has provided good experimental predictions.
The three interactions of the SM will be detailed in the subsections of this chapter. The particles of the SM shown in Figure 2.1 consist of those with a spin of $\frac{1}{2}$, called fermions, and integer spins, called bosons.

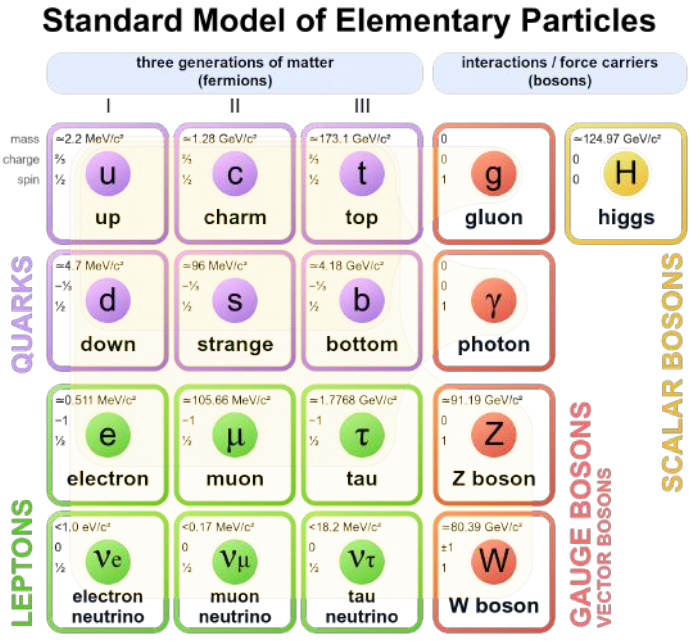

Figure 2.1: The particles in the SM with some of their properties, such as the mass or the electric charge [3].

The fermions are further classified into leptons and quarks, the latter additionally have a colour charge assigned. Both types of fermions come in three generations with different masses. Bosons can be separated into spin-1 and spin-0 bosons (vector and scalar): Gluons (g), photons (γ), Z bosons (Z^0) and W bosons ($W^{\pm}$) are spin-1 particles while the Higgs boson (H) is a spin-0 particle. Another difference is that the photon and gluon are massless while the other three have masses in the range of 80-126 GeV/c^2. Every fermion in the SM has an anti-particle with the same internal quantum numbers but opposite charge, e.g. for an electron e^- the corresponding anti-particle is the positron e^+.
The interaction vertices of the particles in the SM in the weak, strong and electromagnetic interaction can be represented by Feynman diagrams. Figure 2.2 gives an example of the vertices possible in these interactions with the photon γ as the gauge boson for the electromagnetic, the gluon g for the strong and the $W^{\pm}$ or Z boson for the weak interaction.

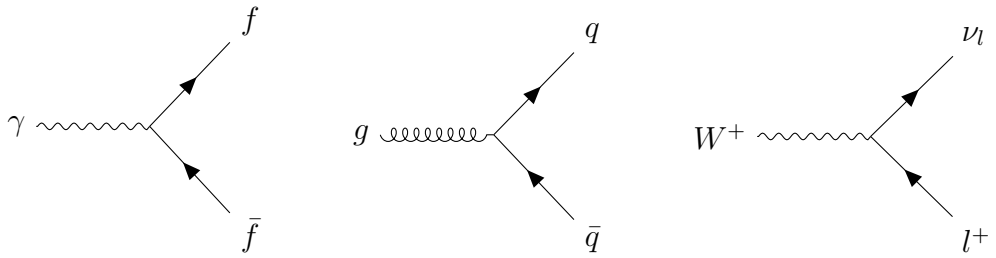

Figure 2.2: Feynman diagrams of the different interactions

2.1 Overview of the Standard Model

The forces interacting between the particles of the SM are described in terms of quantum field theory. Each of the three fundamental forces of the SM can be understood as a local gauge symmetry. For the strong interaction, a local gauge symmetry of $SU(3)_C$ is the group that describes the colour state changes and properties. The electromagnetic and the weak interaction can be unified into the electroweak interaction with a local gauge symmetry of $SU(2)_L \otimes U(1)_Y$ which correspond to weak isospin and hypercharge, respectively.
All in all there is the following local gauge symmetry for the SM:

$$SU(3)_C \otimes SU(2)_L \otimes U(1)_Y, \tag{2.1}$$

with the three fundamental forces described in a unified quantum field theory.
Quantum chromodynamics (QCD) [4, 5] is the theory of the strong interaction, affecting particles interacting under colour charge, namely quarks and gluons. Colour here refers to an arbitrarily named charge analogous to electric charge, but on the basis of three different possible charges: red (r), blue (b) and green (g). Quarks have these three colours, anti-quarks have an anti-colour. There are eight gluons differing in colour, they carry both colour and anti-colour.
The other two interactions of the SM, the electromagnetic and the weak interaction, can be unified in the form of the electroweak interaction [6–9]. At first glance, the electromagnetic and the weak interaction are two separate mechanisms. On one hand, quantum electrodynamics (QED) provides a mathematical theory of the electromagnetic interaction, where only charged particles interact by way of exchanging a massless photon. On the other hand, there is the weak theory which handles any interaction involving the massive spin-1 bosons $W^{\pm}$ with a mass of $m_W = 80.4\,\text{GeV}$ and Z^0 with a mass of $m_Z = 91.2\,\text{GeV}$. The charged current ($W^{\pm}$) is always flavour-changing, while the neutral current (Z^0) is not allowed to be flavour-changing at leading order. With the symmetry group $SU(2)_L \otimes U(1)_Y$ there are four fields, $W^1_\mu, W^2_\mu, W^3_\mu, B_\mu$. The first two are combined to the charged bosons:

$$W^+_\mu = \frac{W^1_\mu + iW^2_\mu}{\sqrt{2}}, \quad W^-_\mu = \frac{W^1_\mu - iW^2_\mu}{\sqrt{2}} \tag{2.2}$$

The latter two mix due to them having the same quantum numbers with the weak mixing angle θ_W [10]:

$$A_\mu = \cos\theta_W B_\mu + \sin\theta_W W^3_\mu \tag{2.3}$$

$$Z_\mu = -\sin\theta_W B_\mu + \cos\theta_W W^3_\mu \tag{2.4}$$

with A_μ identified as the field of the electromagnetic interaction and Z_μ as the field of the Z^0 boson.
For the flavour-changing currents of the weak interaction the probabilities of the different generations of quarks changing into each other are represented using the Cabibbo-Kobayashi-Maskawa matrix, which is an SU(3) matrix with four free, experimentally measured parameters. Also unique to the weak interaction is that in contrast to the electromagnetic and the strong interaction, there can be violations in the symmetry of charge conjugation (C), parity (P) and the combination of both (CP).

2.2 The BEH Mechanism

If gauge invariance is demanded in the SM, the massive bosons do not to have a mass a priori. This contradicts experimental observations. The Brout-Englert-Higgs (BEH) mechanism [11–13] allows the SM to correctly predict massive gauge bosons. It also gives mass to fermions through Yukawa couplings. Parts of the explanations in this chapter are based on a textbook on this subject [14].
This theory can be explained in the form of the Salam-Weinberg model [9] for the electroweak interaction. For that we introduce a doublet of complex scalar fields:

$$\phi = \begin{pmatrix} \phi^+ \\ \phi^0 \end{pmatrix} = \frac{1}{\sqrt{2}} \begin{pmatrix} \phi_1 + i\phi_2 \\ \phi_3 + i\phi_4 \end{pmatrix} \tag{2.5}$$

From the resulting Lagrangian, the mass of the $W^{\pm}$ boson, Z^0 boson and the neutral gauge boson A (which can be identified as the photon) are parameterised as

$$m_W = \frac{1}{2} g_W v \tag{2.6}$$

$$m_z = \frac{1}{2} v \frac{g_W 2}{cos\theta_W} \tag{2.7}$$

$$m_A = 0 \tag{2.8}$$

with g_W as the coupling constant of the $SU(2)_L$ gauge interaction, v as the vacuum expectation value (VEV) of the Higgs field and θ_W as the weak mixing angle. It can be concluded that the spontaneous symmetry breaking of the $SU(2)_L \otimes U(1)_Y$ gives an explanation for the massive gauge bosons and the photon being massless. Feynman diagrams involving the relation between the coupling constants and the boson masses can be seen in Figure 2.3 with $g_Z = g_W / cos\theta_W$.

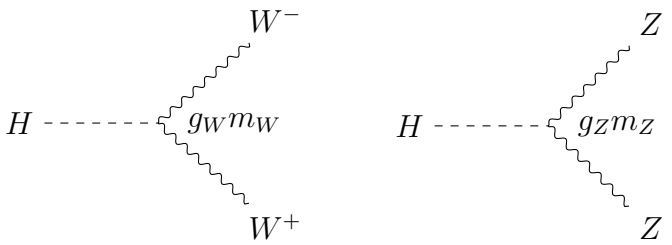

Figure 2.3: The Feynman diagrams involving the equations in (2.6) and (2.7).

Fermions acquire their mass via the Yukawa coupling to the Higgs field:

$$m_f = \frac{1}{\sqrt{2}} g_f v, \tag{2.9}$$

with g_f as the Yukawa coupling constant. The Higgs boson is the quantum excitation of the Higgs field.

2.3 Shortcomings of the Standard Model

A complete theory of the fundamental forces in our universe needs to be able to explain all physical phenomena. The SM is a consistent theory which is able to produce precise experimental predictions regarding the electroweak and the strong interaction, but the theory has limitations. Some of the things not explained by the SM are the phenomenon of dark matter [15], the gravitational force and the hierarchy problem [16].
Dark matter is assumed to make up the majority of mass in the universe. There have been anomalies in the measurements of gravitational density and the rotational speed of galaxies [17], for which the existence of dark matter is a possible explanation. A conclusive theory about all fundamental forces in our universe needs to be able to explain this phenomenon and no particle of the SM is able to explain dark matter.
As already discussed before, the gravitational force is the only fundamental force not included in the SM. Though, not only is the gravitational force not included, it is observed to be 10^{24} times weaker than the weak interaction. This is called the hierarchy problem and there is no explanation in the SM on why there is such a discrepancy between the scales. Tied to that is the previous expectation of the Higgs boson to have been heavier than the one discovered in 2012. This is due to the fact that if the SM is valid up to extremely high mass scales, the quantum loop corrections contributing to the Higgs boson mass would become very large. The hierarchy problem of the Higgs mass could possibly be solved in the Minimal Supersymmetric Model (Chapter 3).

3 The Minimal Supersymmetric Standard Model

Supersymmetry (SUSY) [18] is a popular extension of the SM. It theorizes a symmetry relating the particles of the SM to super-partners (spartners) which would differ by half a unit of spin. The super partners of the fermions are spin-0 scalars (sfermions) and the super-partners of the spin-1 gauge bosons are spin-half gauginos. For the Higgs boson in the MSSM the partners would be a weak isospin doublet of spin-half Higgsinos $\tilde{H}^0_{1,2}$ and $\tilde{H}^{\pm}$. The particles and their spartners as theorized in the Minimal Supersymmetric Model (MSSM) [19] are listed in Figure 3.1. The physical chargino and neutralino states are generally mixtures of the Higgsinos and gauginos.

Particle		Spin		Super-particle		Spin
Quark	q	$\frac{1}{2}$		Squark	$\tilde{q}_L, \tilde{q}_R$	0
Lepton	$\ell^{\pm}$	$\frac{1}{2}$		Slepton	$\tilde{\ell}^{\pm}_L, \tilde{\ell}^{\pm}_R$	0
Neutrino	ν	$\frac{1}{2}$		Sneutrino	$\tilde{\nu}_L, \tilde{\nu}_R(?)$	0
Gluon	g	1		Gluino	$\tilde{g}$	$\frac{1}{2}$
Photon	γ	1	$\tilde{\gamma}$			
Z boson	Z	1	$\tilde{Z}$	Neutralino	$\tilde{\chi}^0_1, \tilde{\chi}^0_2, \tilde{\chi}^0_3, \tilde{\chi}^0_4$	$\frac{1}{2}$
Higgs	H	0	$\tilde{H}^0_1, \tilde{H}^0_2$			
W boson	$W^{\pm}$	1	$\tilde{H}^{\pm}$, $\tilde{W}^{\pm}$	Chargino	$\tilde{\chi}^{\pm}_1, \tilde{\chi}^{\pm}_2$	$\frac{1}{2}$

Figure 3.1: The SM particles and their possible super-partners in the MSSM [14].

3.1 Motivation for Supersymmetry

There are several reasons to introduce Supersymmetry as an extension to the SM (Chapter 2.3). SUSY provides a possible explanation for the phenomenon of dark matter, if the lightest sparticle does not interact electromagnetically and is stable. One such candidate for dark matter would be the neutralino $\tilde{\chi}^0_1$ as a weakly interacting stable particle in many models.

Furthermore, the MSSM is a possible solution to the hierarchy problem of the Higgs boson mass. In a Grand Unified Theory combining the weak, strong and electromagnetic interaction at high mass scales, the Higgs mass would be expected to be higher if applied to the SM due to the corrections of the Higgs mass via quantum loop corrections. Examples of those loops can be seen in Figure 3.2.

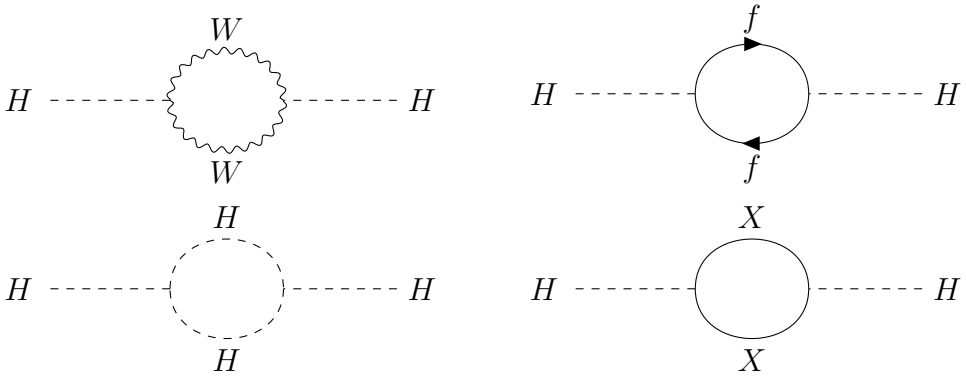

Figure 3.2: Examples for correction loops of the Higgs boson to itself with X representing a new massive particle.

Supersymmetry would solve the hierarchy problem, since every loop of particles would have a corresponding loop of sparticles with the opposite sign. In an exact symmetry with the masses of the corresponding particles being the same they would completely cancel each other out. Since sparticles of the same mass as their particles have not yet been observed, it would fit current expectations that the sparticles are heavier than their partners. If supersymmetry exists, it is a broken symmetry [20] with the sparticles being an unknown amount of mass heavier than the original particles.

3.2 The Higgs Sector of the MSSM

The MSSM [19] is a minimal supersymmetric extension of the SM. Any SUSY theory requires an extended Higgs sector with respect to the SM. In the case of the MSSM, two complex Higgs doublets are assumed. These then break down via electroweak symmetry breaking into five mass eigenstates, $h, H, A, H^{\pm}$. Should CP symmetry be conserved, A would have a CP eigenvalue of -1 while h, H would be neutral bosons and $H^{\pm}$ charged bosons with a CP eigenvalue of $+1$.
Relevant for the Higgs sector is that the MSSM under certain assumptions can be described at tree level completely by the two parameters m_A and $\tan\beta = \frac{<H_d^0>}{<H_u^0>}$, with m_A

being the mass of A and $\tan\beta$ the ratio of the VEV of the down-type doublet to that of the up-type one. Beyond tree level many more relevant parameters are necessary. These additional parameters can be used to define several benchmark scenarios, such as the m_h^{mod+} [21]. In this scenario the top-squark mixing parameter is chosen in such a way that the mass of the h boson is near that of the Higgs boson already discovered at the LHC. A second benchmark scenario is the hMSSM [22]. Here the mass measured for m_h is used to predict the other masses and couplings in the MSSM Higgs sector without taking other parameters of soft symmetry-breaking into account.
Another relevant benchmark scenario is the M_h^{125} scenario [23]. Here, the parameters are chosen such that the mass of m_h, the lightest CP-even Higgs boson, is close to the mass of the particle discovered in 2012 at the LHC [24]. Additionally, the masses of all sparticles are chosen to be heavy enough to not significantly affect the production and decay of the the MSSM Higgs bosons. For high values of $\tan\beta$, the coupling of the heavy Higgs bosons of the MSSM to down-type fermions is enhanced. This leads to a higher branching ratio to e.g. τ leptons and b-quarks. Both of these channels are analyzed at the LHC. Specifically interesting for this thesis is the $H/A \to \tau\tau$ [25] channel studied with the ATLAS detector.

4 The LHC and the ATLAS Detector

4.1 The LHC Accelerator Chain

The Large Hadron Collider (LHC) [26] is the world's largest and most powerful particle accelerator and collider. It was built by the European Organization for Nuclear Research (CERN) between 1998 and 2008 and has a circumference of 27 km in a tunnel underground near Geneva. The particle accelerator was designed to probe the SM at new energy scales and to search for physics beyond the SM with centre-of-mass collision energies as high as 14 TeV and a luminosity of $L = 10^{34}\text{cm}^{-2}\text{s}^{-1}$ for the two high luminosity experiments ATLAS and CMS. There are additional experiments at lower luminosities, such as LHCB for B-physics, TOTEM for detecting protons in elastic scattering at small angles and ALICE for ion experiments.
The LHC is supplied with protons from the injector chain [26] Linac2 (p) - Proton Synchrotron (PS) - Super Proton Synchrotron (SPS) as can be seen in Figure 4.1. After Linac2, the protons have reached an energy of 50 MeV, after the PS up to 25 GeV and after the SPS up to 450 GeV.

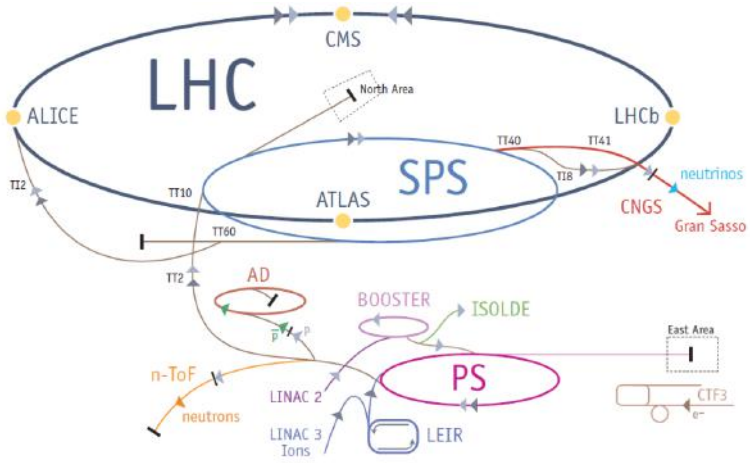

Figure 4.1: Layout of the LHC accelerator chain [27].

4.2 The ATLAS Detector

The ATLAS (A Toroidal LHC ApparatuS) experiment [28] is a general-purpose particle detector at the LHC at CERN. The experiment involves about 3000 physicists from over 180 different institutions. It is designed to observe the high energy particles being accelerated and collided by the LHC and search for possible evidence of physics beyond the SM. Its general layout and main components can be seen in Figure 4.2.

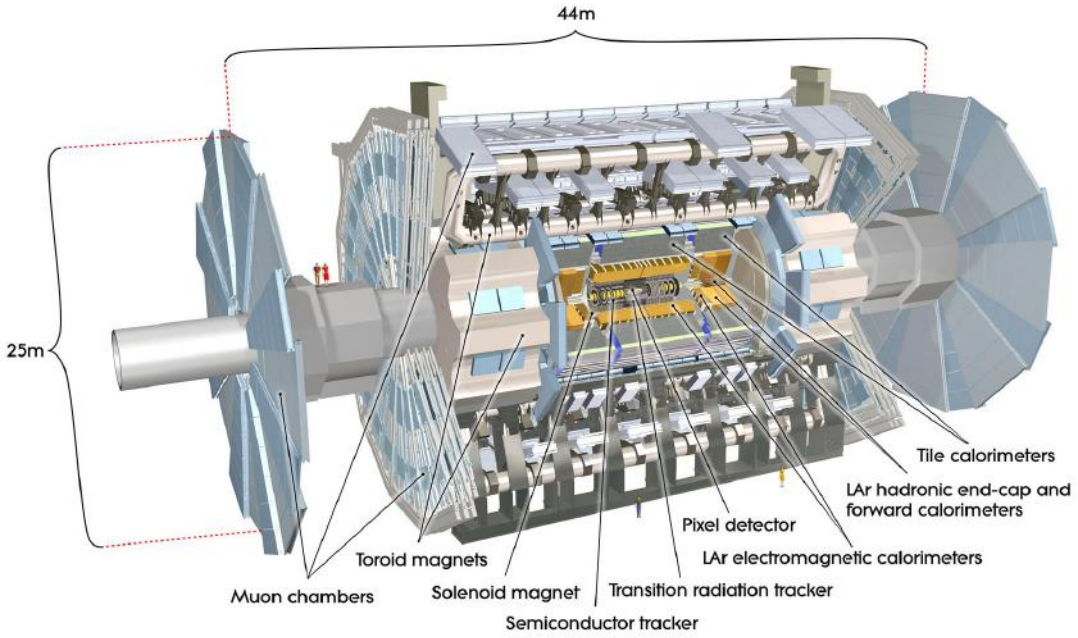

Figure 4.2: Layout of the ATLAS detector [29].

The detector was constructed forward-backward symmetric in respect to the interaction point where the particles accelerated by the LHC collide. The most important components used for particle detection are: The pixel detector, semi-conductor tracker and transition radiation tracker, the three of which make up the inner detector, and the electromagnetic calorimeter, the hadronic calorimeter, the magnet system and the muon spectrometer. Another aspect relevant to its operation is the trigger system.
The coordinate system used to describe the ATLAS detector can be seen in Figure 4.3. It has the nominal interaction point as the origin with the beam direction as the z-axis. The positive x-axis points from the interaction point towards the centre of the LHC ring and the positive y-axis is defined as pointing upwards. Other relevant parameters are the azimuthal angle ϕ which is the angle around the beam axis, the polar angle θ which is the angle from the beam axis and the pseudorapidity which is defined as $\eta = -\ln(\tan(\theta/2))$.

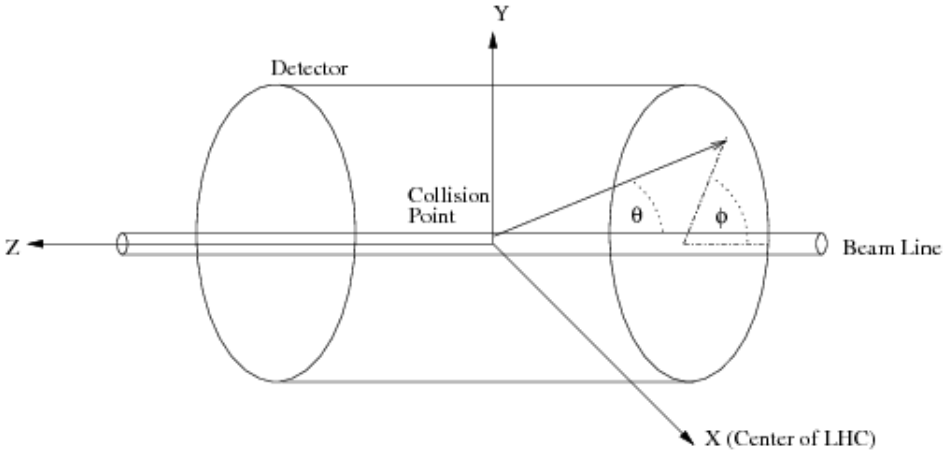

Figure 4.3: Illustration of the ATLAS coordinate system [30].

4.2.1 Inner Detector

The Inner Detector [28] of the ATLAS experiment can be seen in Figure 4.4. It detects the tracks and momenta of charged particles by the way of their interaction with matter at discrete space points. Overall it detects particles within the absolute pseudorapidity range of $|\eta| < 2.5$. A magnetic field surrounds the entire Inner Detector which causes charged particles onto a curved trajectory. The direction and curvature of this curve reveal information about the charge and momentum of the particle. The strength of this magnetic field is about $B = 2$ T and it is produced by the inner solenoid.

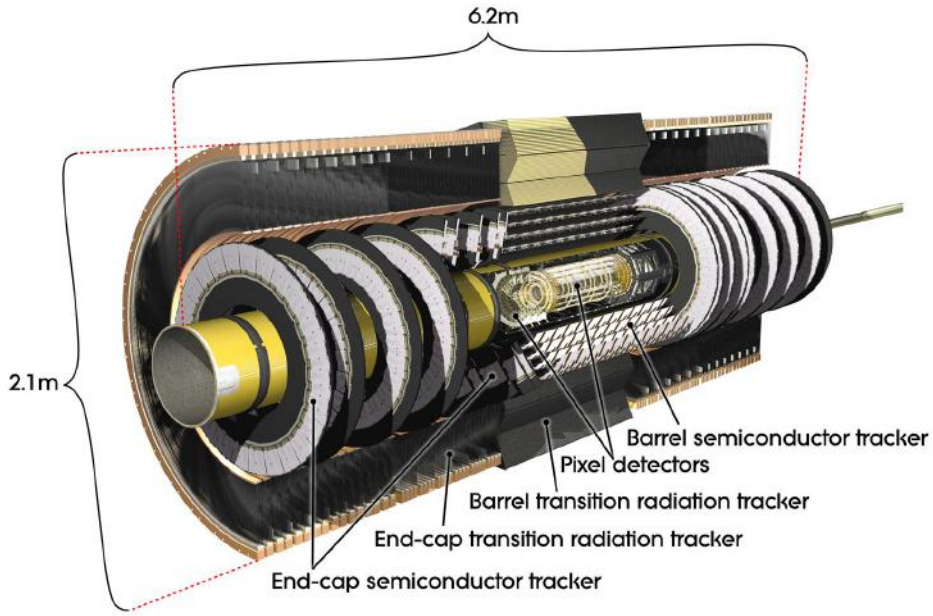

Figure 4.4: Layout of the ATLAS Inner Detector [31].

The two innermost detectors directly bordering the collision chamber are the pixel detector and the semi-conductor detector (SCT). The pixel detector is installed immediately around the collision point with the SCT enveloping it. Both are silicon semiconductor detectors, the first structured as pixels and the second as narrow strips. The pixel detector is designed for very precise tracking. With over 80 million readout channels, it has about half of the total readout channels of the whole detector. The SCT is designed to give a broad spatial cover with two signals from the strips combined to track the space points of particles which pass the detector. Both need to be cooled down to approximately -5 to $-10°$ C to reduce thermal noise. Another challenge is the high radiation environment so close to the beam pipe which reduces the efficiency with continual use. The inner pixel layer needs to be replaced every three years due to radiation damage with the rest being designed to withstand such damage as well as possible.
The outer layer of the Inner Detector is the transition radiation tracker (TRT) made out of gaseous straw tubes interspersed with transition radiation material. Transition radiation is the phenomenon that charged particles going through an interface of materials with different dielectric constants emit radiation whose intensity is proportional to the Lorentz factor $\gamma = \frac{E}{mc^2}$. For this reason, the TRT is very relevant in identifying electrons due to their small mass and therefore high Lorentz factor.
The resolution of the transverse momentum of the Inner Detector is $\frac{\sigma_{pT}}{p_T} = 0.04 \times p_T$ [GeV] [32].

4.2.2 Calorimetry

The calorimetry system [28] is located outside of the solenoidal magnet surrounding the Inner Detector. It detects the energy of the particles going through by absorbing it. Most calorimeters at ATLAS use liquid argon as the active detector medium which is known for its radiation-hardness, its stability over time and its intrinsic linear behavior, while the hadronic calorimeter of the barrel uses scintillating tiles due to the nature of hadronic showers. ATLAS uses sampling calorimeters with alternating layers of absorbing and detecting material to have the particles shower in a short distance and still be able to detect them. The calorimetry system as well as the muon spectrometer are located inside the outer toroidal magnetic field which varies between 0.5 and 1 T.
The electromagnetic calorimeters are in the inner region of the calorimetry system and have lead as the absorbing material and liquid argon as the active material. As the name suggests, it detects particles that shower electromagnetically such as electrons and photons. It has a high energy resolution in the scope of its detection of $|\eta| < 4.9$ with $\frac{\sigma_E}{E} = \frac{10\%}{\sqrt{E}} \bigoplus 0.17\%$ [GeV].

The outer hadronic calorimeter uses steel as the absorber medium, scintillators as the active medium in the barrel and liquid argon as the active medium in the end-caps. It detects particles that shower hadronically. The hadronic calorimeters provide a coverage of up to $|\eta| < 4.9$ with a relative error of $\frac{\sigma_E}{E} = \frac{21\%}{\sqrt{E}}$ [GeV].

4.2.3 Muon Spectrometer

The muon spectrometer [28] makes up the outer part of the ATLAS detector and detects charged particles exiting the calorimeters, measuring their momentum in a pseudorapidity range of $|\eta| < 2.7$. It mainly detects muons, since the other particles are already absorbed by detectors in the inner part of ATLAS. It functions similarly to the Inner Detector with the muons propagating on curved trajectories due to the magnetic field applied through the outer toroids. The muons' trajectories are then detected by Monitored Drift Tubes (MDTs). The drift tubes are isolated from each other with higher granularity used in the innermost plane over $2 < |\eta| < 2.7$ to meet the demanding rate and background conditions.

The precision-tracking chambers detecting the muons are complemented by a system of fast trigger chambers for $|\eta| < 2.4$ which deliver data about the track of the particle going through within nanoseconds. The trigger chambers serve several purposes by providing bunch-crossing identification and well-defined p_T thresholds and measuring the muon coordinates in the direction orthogonal to that determined by the precision-tracking chambers. For tracks of 1 TeV, the p_T resolution is approximately 10%.

4.2.4 Trigger System

The trigger system [28] at ATLAS has two distinct levels: L1 and the High-Level Trigger (HLT). It is designed to select which events happening in the detector are interesting enough to be recorded. Each level refines the previous one and when necessary applies criteria for additional selection.

The L1 trigger is physically implemented in the hardware and uses information from the different detectors implemented in ATLAS. It searches for muons, electrons, photons and jets with a high p_T and also large missing and total transverse energy. The reason for that is that many of the quantities measured have a higher relative accuracy with high transverse momenta. Additionally, lower energy particle physics can be explored by other experiments, and physics with the high energies achievable by the LHC are a novelty. For Run-2 (2015-2018) [33], the instantaneous luminosity was increased to over 10^{34} $\mathrm{cm}^{-2}\mathrm{s}^{-1}$, which required higher trigger rates than previous and an adjustment of the trigger strat-

egy. At the end of Run 2 there was a L1 rate of up to 100 kHz and a HLT rate of approximately 1.2 kHz.

5 Search for the heavy neutral Higgs Boson in the $\tau_{had}\tau_{had}$ Final State

After the discovery of a scalar particle in 2012 at the LHC [24], which was found to be consistent with the theoretical prediction of the SM Higgs boson, the search for new particles beyond the SM continued. As discussed in Chapter 3, the MSSM predicts several undiscovered elementary particles. With a very high centre-of-mass energy, the LHC gives the opportunity to look for these heavy mass resonances.

In the search for the neutral MSSM Higgs bosons H and A, data from ATLAS collected in 2015 and 2018 corresponding to a total integrated luminosity of 139 fb^{-1} was analyzed [34]. At tree level the properties of the Higgs sector in the MSSM depend only on two parameters not already included in the SM, namely the ratio of the VEV of the two Higgs doublets (see Chapter 3.2), $\tan\beta = \frac{<H_d^0>}{<H_u^0>}$, and the mass of the CP-odd Higgs boson, m_A. Beyond tree level, many more parameters define the Higgs sector in the MSSM, some of which might be predictable using the mass of the measured value of the Higgs boson already discovered.

The decay modes for the search are the $H/A \to \tau_{had}\tau_{had}$ and the $H/A \to \tau_{lep}\tau_{had}$ modes. τ_{lep} stands for the leptonic decay of the τ lepton into an electron or muon alongside the respective neutrinos and τ_{had} for the decay into one or more hadrons and a neutrino. For this search, a mass resonance of $0.2 - 2.5$ TeV and $\tan\beta$ of $1 - 58$ was considered. This thesis will focus on the $\tau_{had}\tau_{had}$ final state. The production modes taken into account for the h, A and H Higgs bosons were the gluon-gluon fusion and production in association with b-quarks. The leading-order Feynman diagrams for these production modes are shown in Figure 5.1.

5.1 Event Reconstruction and Selection

For the $\tau_{had}\tau_{had}$ mode to be analyzed, the particles that result from these modes and their energies need to be reconstructed [25]. The jets occurring in the detector are re-

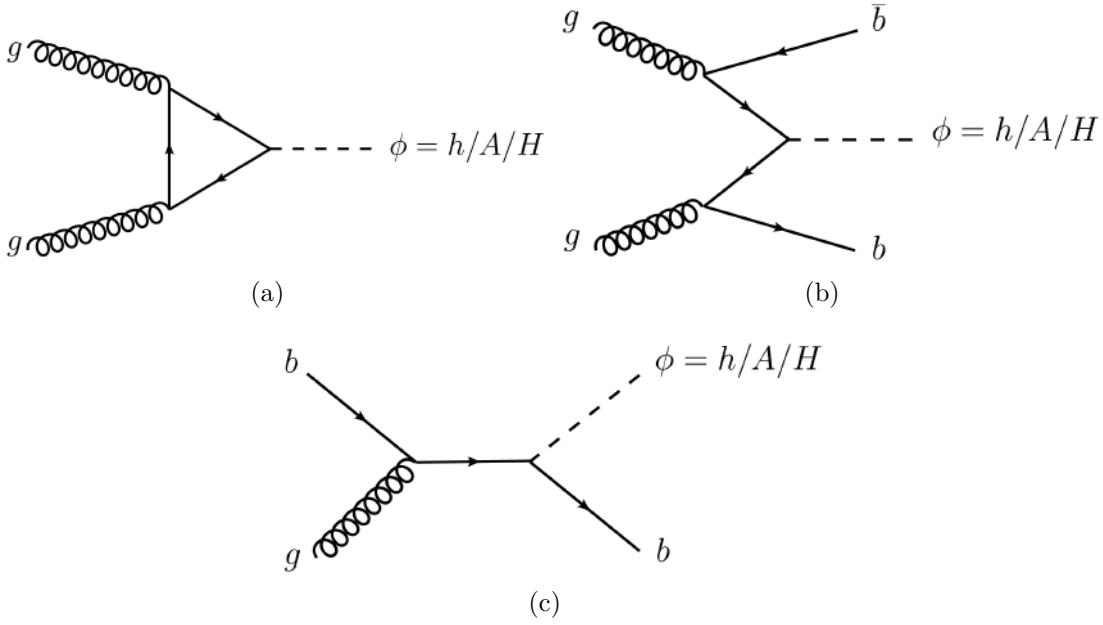

Figure 5.1: Leading-order Feynman diagrams for (a) gluon-gluon fusion and b-associated production of neutral MSSM Higgs boson with (b) four-flavour and (c) five-flavour schemes [25].

constructed from topological clusters of energy deposits in the calorimetry system using the anti-k_t algorithm [35] with a radius parameter value of $R = 0.4$. For this they are required to have $p_T > 20$ GeV and $|\eta| < 2.5$. Additionally a multivariate tagger is used to determine the likelihood for the jet being contaminated by pile-up. In order to identify jets which contain b-hadrons (b-jets), a multivariate algorithm is employed based on the presence of tracks with large impact parameters with respect to the primary vertex, the presence of displaced secondary vertices and the reconstructed flight paths of b- and c-hadrons associated with the jet. By the use of this method, the algorithm reaches an efficiency of 70% for identifying b-jets and rejections between 13 and 380 for the different types of other jets [36].

Hadronic τ lepton decays consist of a neutrino and a set of visible decay products ($\tau_{\text{had-vis}}$), usually one or three charged pions and a number of neutral pions with decreasing probability. The jets of those visible decay products are the starting point for the reconstruction. The $\tau_{\text{had-vis}}$ candidates are required to have $|\eta| < 2.5$ as well as $p_T > 45$ GeV. With a Boosted Decision Tree (BDT) reconstruction procedure to reject background jets, the efficiency of reconstructing $\tau_{\text{had-vis}}$ candidates is 95% with a background rejection between 20 and 200, depending on the pseudorapidity of the $\tau_{\text{had-vis}}$ candidate. Lastly the missing transverse energy, $\boldsymbol{E}_T^{miss}$, is calculated as the negative vectorial sum of the $\boldsymbol{p}_T$ of all the reconstructed objects.

The $\tau_{had}\tau_{had}$ channel events [25] are recorded using single τ triggers with a p_T threshold of 80, 125 or 160 GeV depending on the data taking period. Event candidates must have a minimum of two $\tau_{\text{had-vis}}$ candidates with $p_T > 65$ GeV and no identified electrons or muons. The $\tau_{\text{had-vis}}$ candidate with the highest p_T must be geometrically matched to the trigger signature and exceed the trigger p_T threshold by 5 GeV. The two leading $\tau_{\text{had-vis}}$ candidates must pass the "medium" and "loose" identification criteria respectively and need to have opposite electric charge and be back to back in the transverse plane. Events containing at least one jet originating from a b-quark are placed in a b-tag category while events with no such jets are placed into a b-veto category.

5.2 Background Estimation Methods

In the $\tau_{had}\tau_{had}$ channel the dominant background contribution comes from multijet production, the estimation of which is described in Chapter 5.2.1. Other important background contributions arise from $Z/\gamma^* \to \tau\tau$ production in the b-veto category or $t\bar{t}$ production in the b-tag category with less important backgrounds being $W(\to \ell\nu)$+jets, single t-quark and $Z/\gamma^*(\to \ell\ell)$+jets production.
These latter contributions are estimated via simulation, to which corrections are applied to take mismodelling of the trigger, reconstruction, identification and isolation efficiencies, the electron to $\tau_{\text{had-vis}}$ misidentification rate and the momentum scales and resolutions into account. This sample of simulated events is then normalised using the theoretical cross sections of these processes and the integrated luminosity of the data gathered. To improve the modelling for the $W+$ jets and $t\bar{t}$ background, the jets that are misidentified as $\tau_{\text{had-vis}}$ candidates are weighted by fake-rates measured in the respective control regions in data to provide a partly data-driven background estimate.

5.2.1 The Fake-Factor Method

In the $\tau_{had}\tau_{had}$ channel the dominant background contribution is from multijet production, which is estimated by a data-driven technique using what is called the fake-factor method [25]. In it, contributions of multijet events in the signal region (SR) of the channel are estimated using events in two control regions (CR1 and DJ-FR). In the CR1 region the leading $\tau_{\text{had-vis}}$ candidate passes the τ identification criteria and the subleading $\tau_{\text{had-vis}}$ candidate fails it and in the DJ-FR a jet trigger must have fired instead of the single τ trigger and the $\tau_{\text{had-vis}}$ candidate matched to it is required to fail the identification (Figure 5.2). Events in the DJ-FR (the dijet fake-regions) are used to measure fake-factors (f_{DJ}), which are defined as the ratio of the number of $\tau_{\text{had-vis}}$ candidates that pass the "loose"

identification to those that fail said identification. These fake-factors are then used to weight the events in the other control region CR1 to estimate the multijet contribution:

$$N^{SR}_{multijet} = f_{DJ} \times (N^{CR1}_{data} - N^{CR1}_{non-MJ})$$

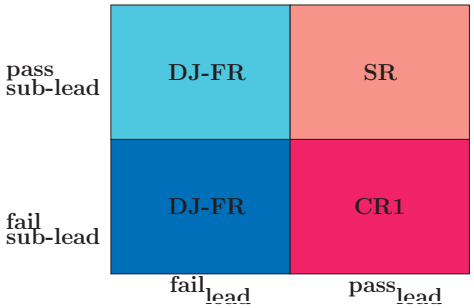

Figure 5.2: Diagram of the DJ-FR and CR1 control regions.

Overall the purity of multijet events in the DJ-FR is 98-99% for the b-veto and 93-98% for the b-tag category. The non-multijet contamination is then subtracted via simulation. The fake-factors involved are seen in Figure 5.3. They are calculated dependent on the p_T of the subleading $\tau_{\text{had-vis}}$ candidate. One-track refers to one charged pion in the decay products and three-track to three charged pions.

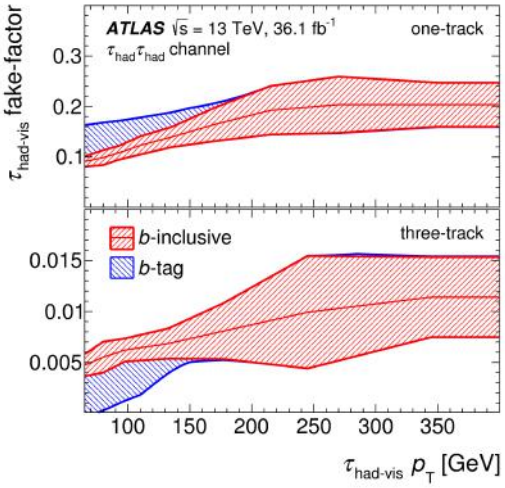

Figure 5.3: The $\tau_{\text{had-vis}}$ identification fake-factors in the $\tau_{had}\tau_{had}$ channel as a function of the p_T of the subleading $\tau_{\text{had-vis}}$ candidate. The red band signals the total uncertainty in the b-inclusive or b-veto selection and the blue band the additional uncertainty in a b-tag selection [25].

5.3 Systematic Uncertainties in the $\tau_{had}\tau_{had}$ and $\tau_{lep}\tau_{had}$ channel

Uncertainties in the simulated signal and background contributions are taken into consideration in the statistical analysis. The main systematic uncertainties are shown in Figure 5.4. They arise from the determination of the $\tau_{\text{had-vis}}$ identification efficiency and energy scale, estimation of the backgrounds with misidentified $\tau_{\text{had-vis}}$ candidates and the modelling of Z+jets background and also depend on the masses of the potential BSM Higgs bosons.

Source	ggF (400 GeV)	ggF (1 TeV)	bbH (400 GeV)	bbH (1 TeV)
Tau id. efficiency	0.14	0.16	0.12	0.08
Tau energy scale	0.33	0.09	0.22	0.03
Z+jets bkg. modeling	0.27	0.19	0.08	0.04
Mis-id. $\tau_{\text{had-vis}}$ bkg.	0.22	0.01	0.14	0.03
Others	0.09	0.04	0.11	0.02
Total	0.54	0.28	0.45	0.13

Figure 5.4: Relative increase in the expected 95% CL upper limits for the production cross section times branching fraction relative to the statistical only expected limit for each systematic uncertainty under consideration, shown for scalar bosons with mass of 400 GeV and 1 TeV produced via ggF and bbH production [34].

For the multijet background and its estimation method, the uncertainty is related to the number of events in the DJ-FR and from the subtraction of the non-multijet contamination, with an additional uncertainty arising from the application of the fake-factors in the b-tag category, which accounts for changes in the composition of the jet with respect to the inclusive selection of the DJ-FR [25].

5.4 Results in the Search for the heavy neutral Higgs Boson at ATLAS

In the most recent analysis of both the $\tau_{lep}\tau_{had}$ and $\tau_{had}\tau_{had}$ channel [34] based on data corresponding to an integrated luminosity of 139 fb^{-1} at $\sqrt{s} = 13$ TeV, the data was found to be in good agreement with the background predicted by the SM.
In the benchmark scenario M_h^{125} [23] for the parameters below tree level, the mass of

the lightest CP-even Higgs boson is chosen close to 125 GeV. Moreover the masses of all the spartners are heavy enough to affect the production and decay of the MSSM Higgs bosons only slightly. For large values of $\tan\beta$, the coupling of the MSSM Higgs bosons to down-type fermions would be enhanced, leading to increased branching ratios into τ leptons and b-quarks. In this analysis, the H and A MSSM Higgs bosons masses are treated as degenerate, since the experimental resolution did not allow a differentiation with the symbol ϕ referring to them both.

The results for the cross section times the branching fraction of the ϕ boson decaying into two τ leptons can be seen in Figure 5.5 (a) and (b). Upper limits on the cross section times branching fraction for Φ are set at a confidence level (CL) of 95% as a function of the boson mass.

The data was interpreted in terms of the MSSM. In Figure 5.5 (c) the exclusion regions in the $m_A - \tan\beta$ plane excluded at 95% CL in the benchmark scenario M_h^{125} can be seen. It can be concluded that no significant deviation from the SM background has been observed.

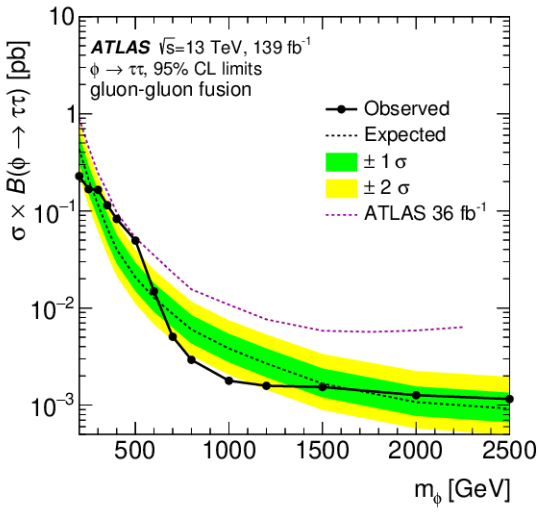

(a)

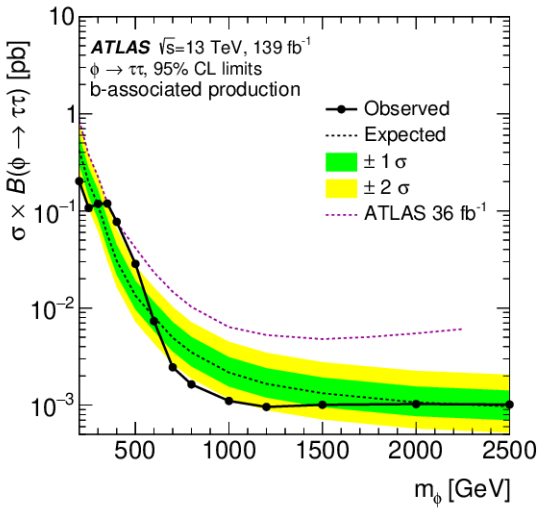

(b)

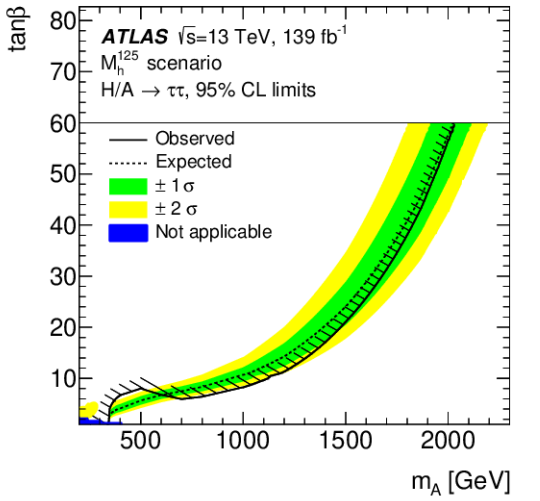

(c)

Figure 5.5: Production cross section times branching fraction for a scalar boson (Φ) produced via (a) gluon-gluon fusion and (b) b-associated production as a result of both the $\tau_{had}\tau_{had}$ and $\tau_{lep}\tau_{had}$ channel. The dotted line represents the excluded region from the 2015-2016 data ATLAS search [25]. The 95% confidence levels on $\tan\beta$ are shown in (c) as a function of m_A [34].

6 Improvements to the Fake-Factor Method

The fake-factor method explained in Chapter 5.2.1 has been used in the ATLAS analysis to estimate the multijet background contribution in the $H/A \to \tau_{had}\tau_{had}$ and $H/A \to \tau_{lep}\tau_{had}$ channels [25, 34]. The aim of this Bachelor thesis is to evaluate a possible improvement to this method to get a better multijet background estimate by implementing a second dimension additional to the p_T of the subleading $\tau_{\text{had-vis}}$ candidate for the fake-factor to depend on. A better modelling of the multijet background would lead to a more precise modelling of the different variables in the signal region. This analysis was conducted for two different τ lepton identification algorithms currently used by ATLAS analyses.

6.1 BDT- and RNN-ID

Since τ leptons have a proper decay length of 87 μm [37], they cannot be directly measured in the ATLAS detector and particle identification is achieved via reconstruction from their decay products. In the case of the hadronic τ lepton decay, the reconstruction involves a jet with one or three charged pions in most cases, as well as possibly additional neutral pions present. These jets are similar to other jet events occurring at the detector and therefore an identification algorithm is needed to decide whether such a jet likely originates from a τ lepton or not.

In the analysis using $\sqrt{s} = 13$ TeV with 139 fb^{-1} by the ATLAS collaboration of the $H/A \to \tau\tau$ channel [34], a Boosted Decision Tree (BDT) ID [38] was used. In this algorithm several discriminating variables were used to differentiate between the decay products of real τ leptons and random jets. These variables are: The central energy fraction, the leading track momentum fraction, the track radius, the leading track IP significance, the number of tracks in the isolation region, the maximum ΔR, the transverse flight path significance, the track mass, the track-plus-π^0-system mass, the number of π^0 mesons and the ratio of track-plus-π^0-system p_T [38]. There are separate algorithms for the one-prong (1P) and three-prong (3P) $\tau_{\text{had-vis}}$ candidates.

The "loose" τ identification criterion which is relevant for the fake-factor method has an efficiency of about 85% for the 1P $\tau_{\text{had-vis}}$ candidates and 75% for the 3P $\tau_{\text{had-vis}}$ candidates, while the rejection factors for these criteria are about 12 for the 1P tracks and 61 for the 3P tracks [38].

In Figure 6.1, plots of the fake-factor depending on p_T of the subleading $\tau_{\text{had-vis}}$ candidate are shown passing the "loose" criterion in the BDT-ID in the 1P and 3P as well as the opposite sign (OS) and same sign (SS) regions, where OS refers to the two candidates having an opposite charge and SS to the same one.

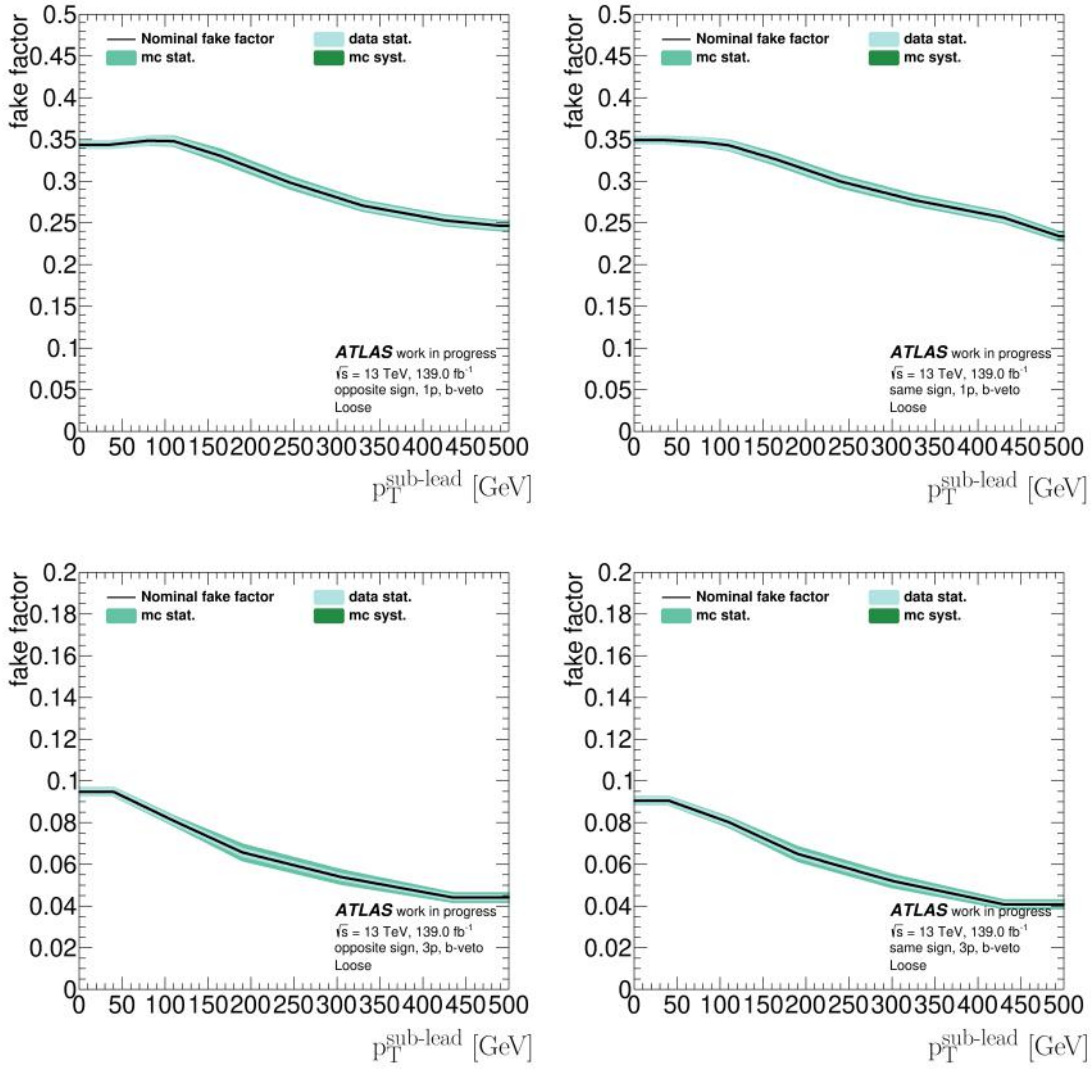

Figure 6.1: The dependence of the fake-factor on p_T of the subleading τ candidate in the 1P/3P and OS/SS regions based on the BDT τ-ID with error bands including the statistical error on the data and the statistical error on the MC simulation.

The Recurrent Neural Network (RNN) [39] identification is a novel τ identification algorithm. The RNN-ID uses a combination of low-level input variables for individual tracks and clusters, which are associated to the $\tau_{\text{had-vis}}$ candidates in addition to several high-level observables calculated from track and calorimeter quantities. The relevant information from the individual tracks include the transverse momentum, the transverse and longitudinal impact parameters, the angular distance to the $\tau_{\text{had-vis}}$ axis and the number of hits on the track in the different silicon layers of the Inner Detector. From the clusters, the transverse energy and the angular distance of the $\tau_{\text{had-vis}}$ axis cluster moments to its respective tracks are used, the last of which includes the cluster depth, the longitudinal cluster extension and the radial cluster extension.
The RNN τ identification was trained using simulated samples of $\tau_{\text{had-vis}}$ candidates. True candidates from $Z/\gamma^* \to \tau\tau$ were required to be geometrically matched to candidates at generator level and then correctly reconstructed as 1P or 3P decays. Candidates not originating from true τ lepton decays were taken from simulated dijet samples and then required to be reconstructed as 1P or 3P candidates. Due to the distinct nature of the 1P and 3P tracks there is a dedicated algorithm to each of those cases.
The RNN-ID has for the "loose" identification criterion a signal efficiency of 85% for 1P tracks and 75% for 3P tracks as well as a background rejection of 21 for 1P and 90 for 3P. In direct comparison to the BDT-ID, the RNN-ID has roughly twice the signal efficiency for the same background rejection.
Figure 6.2 shows the dependence of the fake-factor on the p_T of the subleading $\tau_{\text{had-vis}}$ candidate passing the "loose" criterion in the RNN-ID in the 1P and 3P as well as the OS and SS regions. The uncertainties in the fake-factor are larger here than in the BDT-ID, since the higher background rejection in the RNN-ID at the same signal efficiency leads to less fake $\tau_{\text{had-vis}}$ candidates, increasing the statistical uncertainty on the fake-factor.

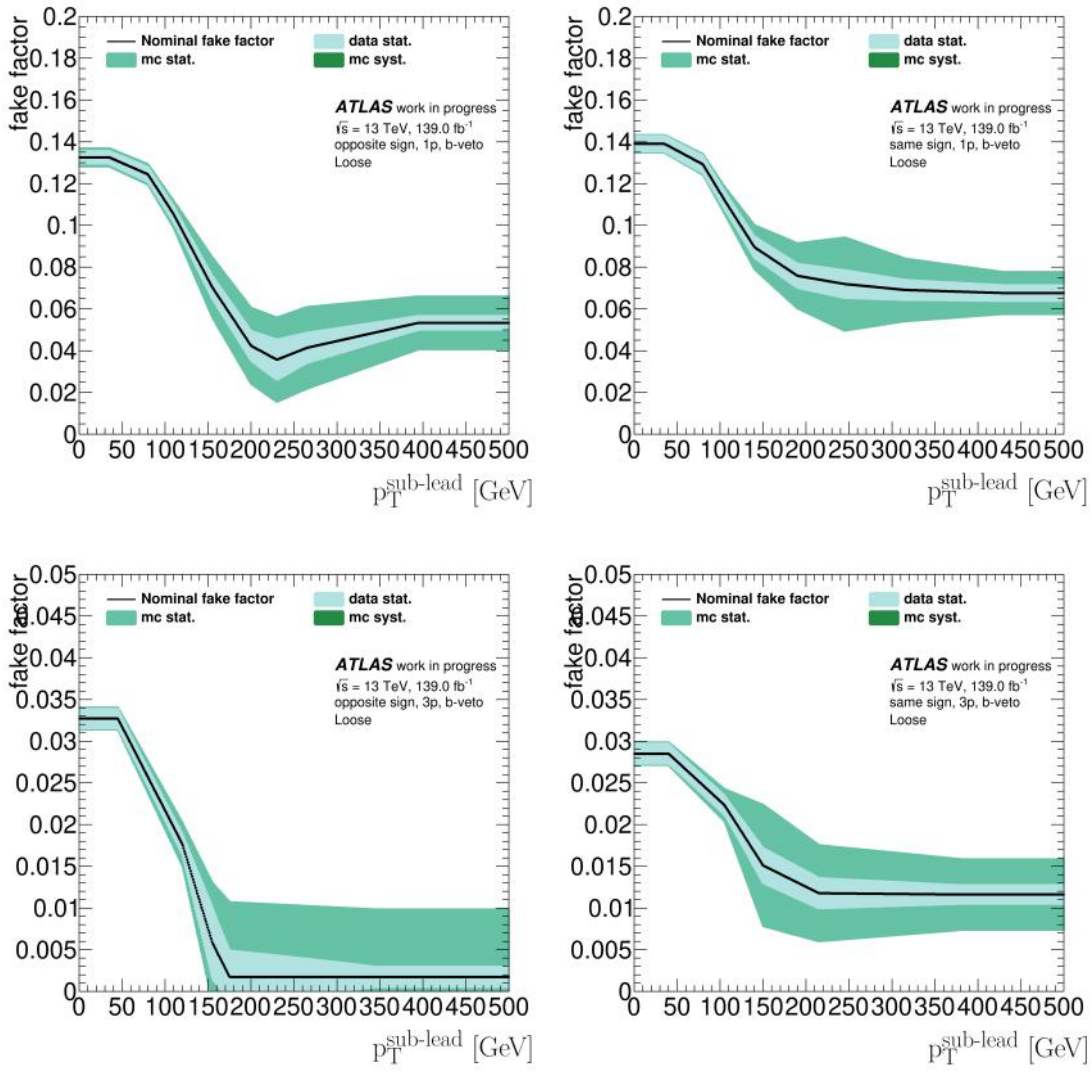

Figure 6.2: Plots of the fake-factor depending on p_T of the subleading τ candidate in the 1P/3P and OS/SS regions based on the RNN τ-ID with error bands including the statistical error on the data and the statistical error on the MC simulation.

6.2 Motivation and Implementation 2d-Binning Method

The aim of the fake-factor method is to give an optimal background modelling in the signal region of the analysis, where both the leading and the subleading $\tau_{\text{had-vis}}$ candidates have an opposite charge and pass the τ-ID. Since the background modelling cannot be evaluated in the signal region due to a possible signal contamination, it is instead evaluated in the validation region, where both $\tau_{\text{had-vis}}$ candidates pass the τ-ID, but have the same charge. Only when the modelling is fixed based on the modelling in the validation region it is applied for the analysis in the signal region.
The current implementation of the fake-factor method uses the definition of the DJ-FR as the region where the leading $\tau_{\text{had-vis}}$ candidate fails the "loose" identification and CR1 as the region where the leading $\tau_{\text{had-vis}}$ candidate passes the aforementioned ID and the subleading one fails it. The fake-factor is then evaluated separately for 1P and 3P $\tau_{\text{had-vis}}$ candidates and calculated dependent on the p_T of the subleading $\tau_{\text{had-vis}}$ candidate.
The BDT-ID is about the be replaced by the RNN-ID for future analyses. The improvements to the fake-factor which are the subject of this thesis will be conducted in both these ID algorithms.
Possible improvements to the fake-factor method involve e.g. revisiting the definition of the control regions DJ-FR and CR1, the choice of another variable other than the p_T of the subleading $\tau_{\text{had-vis}}$ candidate on which the fake-factors depend, improvements to the identification algorithm or introduction of a new identification algorithm altogether and the addition of a second dependence in the calculation of the fake-factors in an additional variable. Some of these, like the conception of a complete new identification algorithm, are beyond the scope of a Bachelor thesis. The implementation of a second variable on which the fake-factors can depend, in addition to the p_T of the subleading $\tau_{\text{had-vis}}$ candidate, was investigated.
For the implementation of the 2d binning of the fake-factor, it needed to be decided which variable to use in addition to the p_T of the subleading $\tau_{\text{had-vis}}$ candidate. The pseudorapidity η of the subleading $\tau_{\text{had-vis}}$ candidate is the variable on which the fake-factor has the next largest dependence and since it is a symmetrical variable, the absolute value was used to achieve lower statistical uncertainty. Figure 6.3 shows the dependence of the fake-factor in $|\eta|$ of the subleading $\tau_{\text{had-vis}}$ candidate in the 1P/3P and OS/SS regions in the BDT-ID. It can be seen that the fake-factor has a dependency on $|\eta|$. Note that systematic uncertainties on the fake-factors have not yet been taken into account.

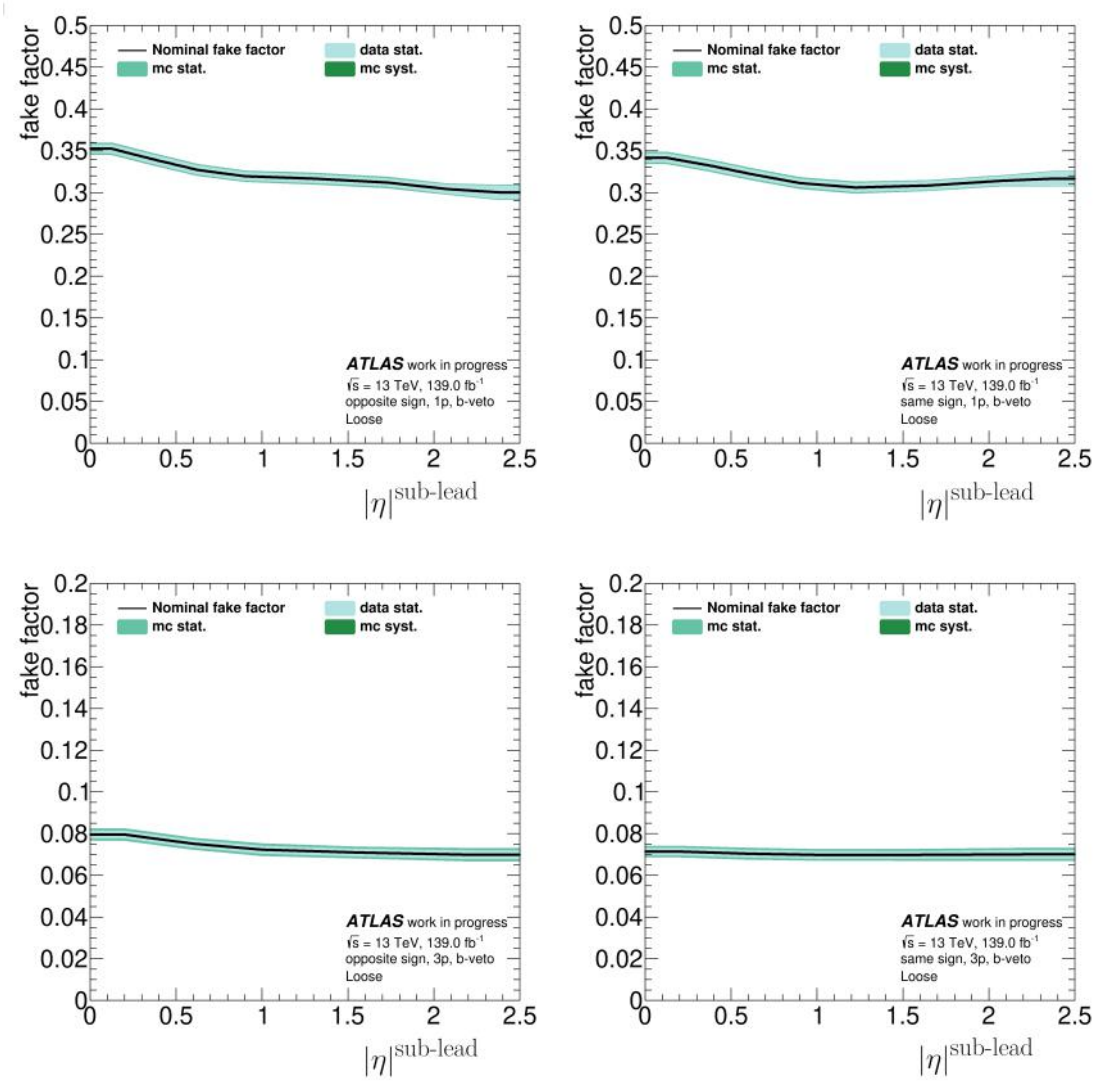

Figure 6.3: The fake factor depending on $|\eta|$ of the subleading τ candidate in the 1P (upper row)/3P (lower row) and OS (left)/SS (right) regions based on the BDT τ-ID with error bands including the statistical error on the data and the statistical error on the MC simulation.

For the RNN-ID, the $|\eta|$ of the subleading $\tau_{\text{had-vis}}$ candidate was also the best variable to calculate the fake-factor in dependence on next to its p_T. Figure 6.4 shows the dependence of the fake-factor on $|\eta|$ in the 1P (upper row)/3P (lower row) and OS (left)/SS (right) regions. It can be seen that the RNN fake-factor has higher statistical errors than the BDT. Because of this, it is not clear whether there is a real dependency of the fake-factor on $|\eta|$, especially since the systematic errors are not yet included.

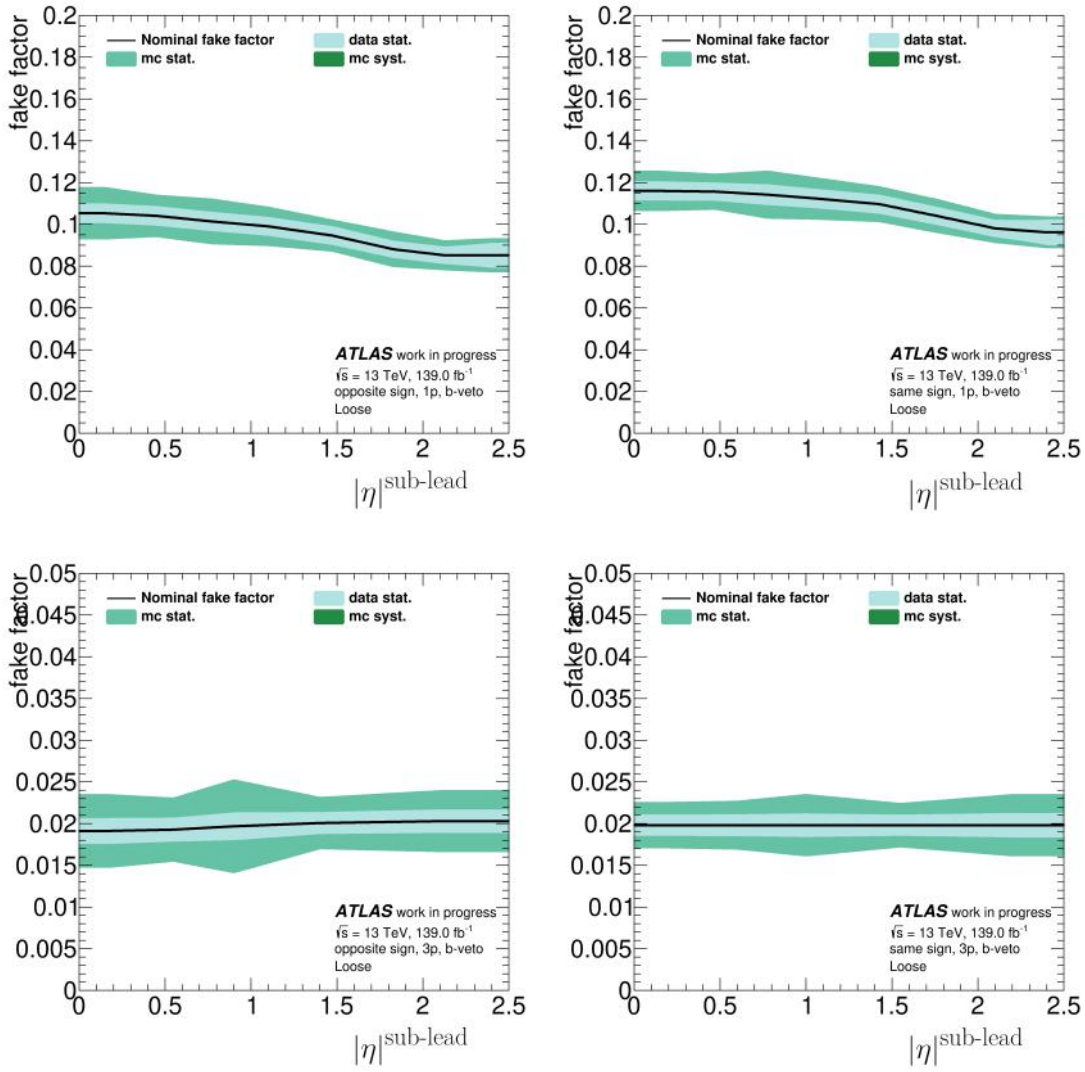

Figure 6.4: The fake factor depending on $|\eta|$ of the subleading τ candidate in the 1P (upper row)/3P (lower row) and OS (left)/SS (right) regions based on the RNN τ-ID with error bands including the statistical error on the data and the statistical error on the MC simulation.

Due to these plots it was decided to evaluate the fake-factor in two bins of $|\eta|$ of the subleading $\tau_{\text{had-vis}}$ candidate, with the first being $0 < |\eta| < 1.5$ and the second $1.5 < |\eta| < 2.5$.

This also matches the geometry of the ATLAS detector with the lower $|\eta|$ slice covering the barrel region and the higher $|\eta|$ slice covering the end-cap region of the electromagnetic calorimetry [28].
The separation of the fake-factor in dependence of p_T of the subleading $\tau_{\text{had-vis}}$ candidate in these higher and lower $|\eta|$ bins in the BDT-ID can be seen in Figure 6.5, were the two different bins for the same regions are shown in opposition with the 1P/OS region in the upper row and the 3P/SS region in the lower row. The regions are chosen as such because the 3P/OS region does not contain enough data for an application of the fake factor. The curves are similar to each other, but not identical within the uncertainties shown.
The corresponding plots can be seen in Figure 6.6, but with the RNN-ID. Again the statistical error is more relevant than in the BDT-ID. It is worth noting that the difference between the two slices of $|\eta|$ are more significant in the 1P/OS region than in the 3P/SS one and thus it appears that including a second variable on which the fake-factor depends would improve the modelling in the opposite sign regions more than in the same sign regions. Note again that systematic uncertainties to the fake-factors have not yet been included.

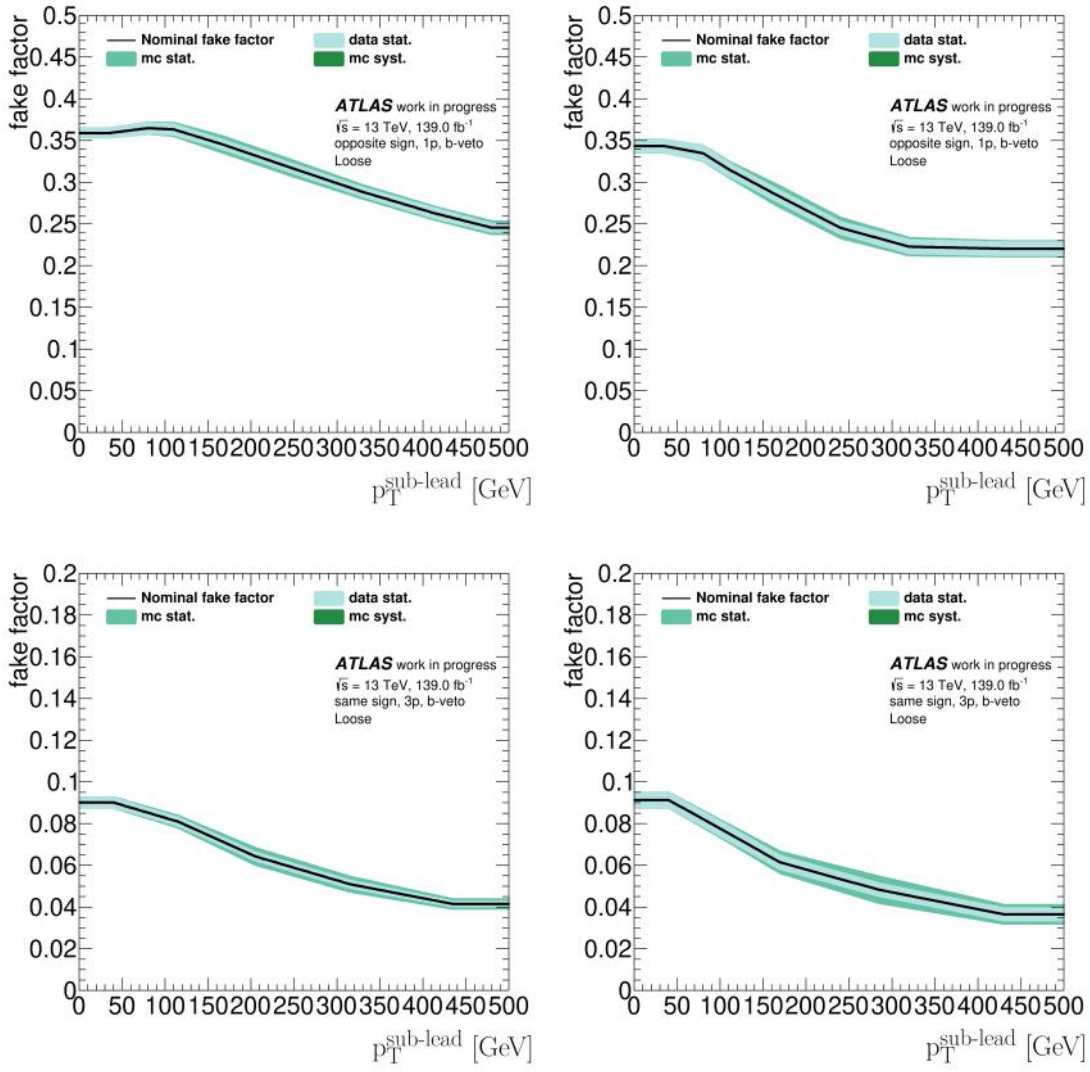

Figure 6.5: p_T dependencies of the fake-factor in slices of $|\eta|$ with the 1P/OS region in the upper plots and the 3P/SS region in the lower plots in the binning of lower $|\eta|$ (left) and higher $|\eta|$ (right) in the BDT-ID with error bands including the statistical error on the data and the statistical error on the MC simulation.

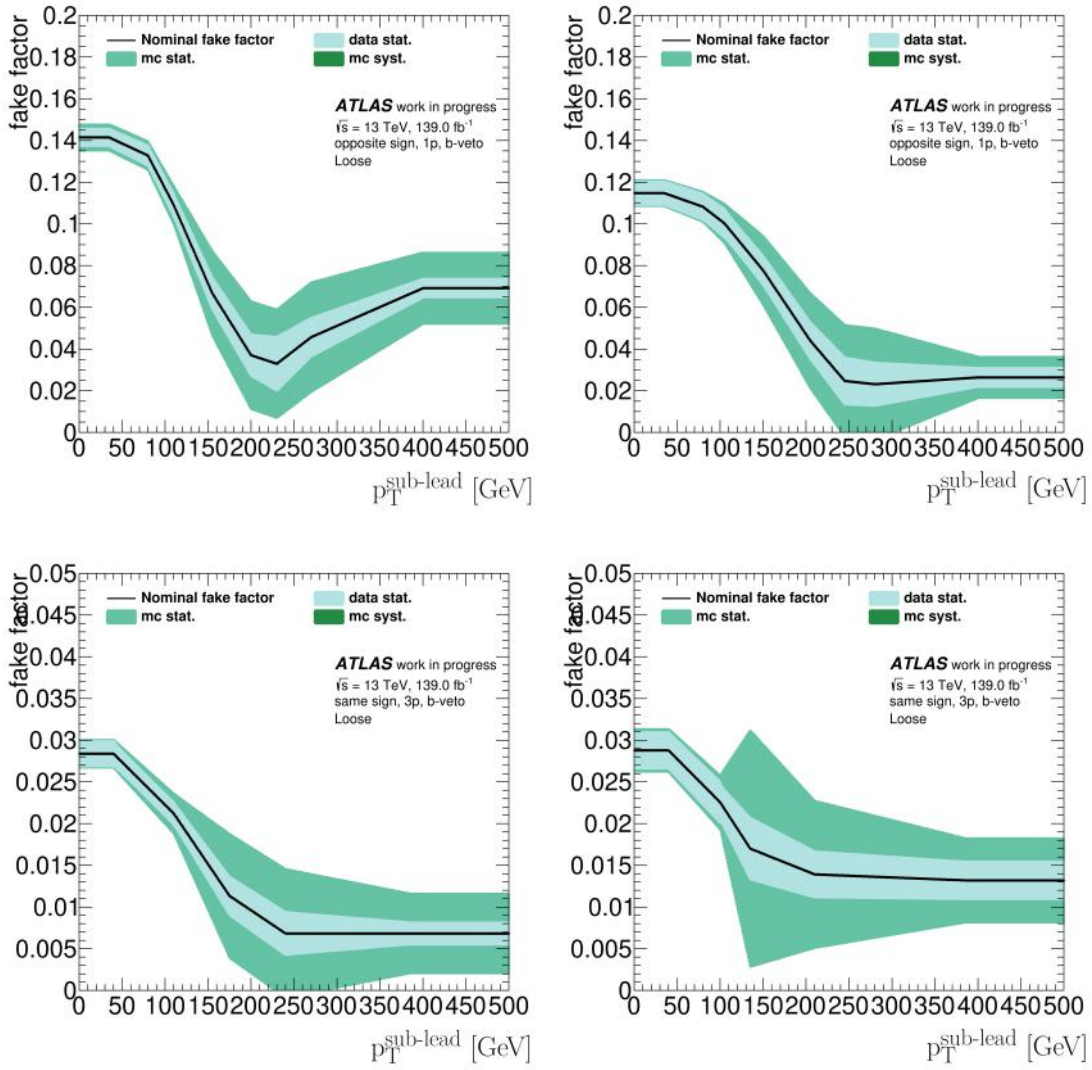

Figure 6.6: p_T dependencies of the fake-factor in slices of $|\eta|$ with the 1P/OS region in the upper plots and the 3P/SS region in the lower plots in the binning of lower $|\eta|$ (left) and higher $|\eta|$ (right) in the RNN-ID with error bands including the statistical error on the data and the statistical error on the MC simulation.

6.3 Results

An important variable in the $H/A \rightarrow \tau\tau$ channel is the total transverse mass m_T^{tot}. The transverse mass of two τ leptons originating from the same decay is defined as $m_T^{tot} \equiv \sqrt{(p_T^{\tau_1}+p_T^{\tau_2}+E_T^{miss})^2 - (\boldsymbol{p}_T^{\tau_1}+\boldsymbol{p}_T^{\tau_2}+\boldsymbol{E}_T^{miss})^2}$ with E_T^{miss} as the missing transverse energy. Its relevance stems from the fact that the neutrinos from the τ lepton decays make an exact reconstruction of the resonance's mass impossible.

Distributions of m_T^{tot} in the validation region can be seen in Figure 6.7 with the upper plots showing the modelling based on the BDT-ID and the lower plots showing the modelling based on the RNN-ID. The plots on the left show the one-dimensional fake-factor modelling while the plots on the right show the fake-factor with a second dependence of $|\eta|$ of the subleading $\tau_{\text{had-vis}}$ candidate.

By eye, it cannot be determined whether the introduction of a two-dimensional binning of the fake-factor results in any improvements of the multijet background estimate in either ID. In the difference of the BDT-ID and the RNN-ID it can be noted that the usage of the RNN-ID results in less overall multijet background. The uncertainties of the fake-factor for the RNN-ID are larger, but they are applied to a smaller background. Therefore, the absolute uncertainties on the background may be smaller with RNN-ID than with the BDT-ID.

In addition to m_T^{tot}, plots of the p_T and $|\eta|$ of the subleading $\tau_{\text{had-vis}}$ candidate can be found in the appendix in Figure A.1 for the BDT-ID and Figure A.2 for the RNN-ID.

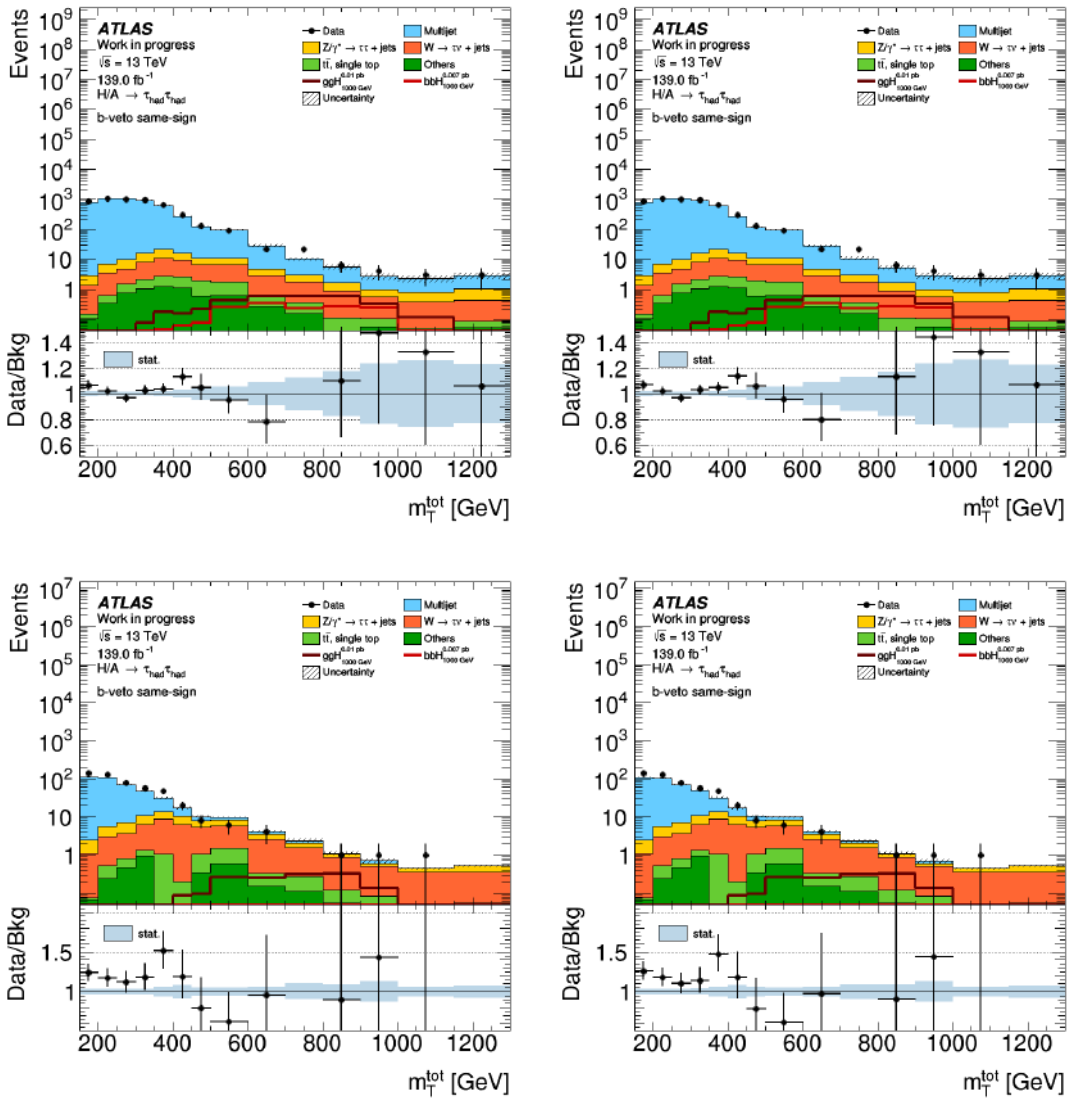

Figure 6.7: Plots of m_T^{tot} in the validation region without binning of the fake factor in $|\eta|$ (left) and with binning of the fake factor (right) based on BDT τ-ID (upper row) and RNN τ-ID (lower row)

To be able to make quantitative statements about the implications of the two-dimensional fake-factor on the modelling of the multijet estimate, a χ^2-test [40] was performed. A χ^2-test is a statistical hypothesis test which provides a way to measure how well a distribution fits the null hypothesis. The formula to compare an unweighted histogram with a total number of events of $N = \sum_{i=1}^{r} n_i$ to a weighted histogram with a total number of events of $W = \sum_{i=1}^{r} w_i$ is

$$\chi^2 = \sum_{i=1}^{r} \frac{(n_i - N\tilde{p}_i)^2}{N\tilde{p}_i} + \sum_{i=1}^{r} \frac{(w_i - W\tilde{p}_i)^2}{s_i^2}$$

,

with s_i as the sum of squares of weights of events in the i-th bin and $\tilde{p}_i$ as the maximum likelihood estimator defined as $\tilde{p}_i = (Ww_i - Ns_i^2 + \sqrt{(Ww_i - Ns_i^2)^2 + 4W^2 s_i^2 n_i})/(2W^2)$. The results of the χ^2-test divided by the respective number of freedoms (NDF) of all the histograms in the three variables, the one-dimensional and two-dimensional modelling and the two IDs can be seen in Table 6.1.

Table 6.1: χ^2/NDF values of the IDs with and without the additional dependence

Variable	BDT (without)	BDT (with)	RNN (without)	RNN (with)
m_T^{tot}	1.29	1.26	0.81	0.81
p_T (subl. τ)	2.06	2.03	1.75	1.74
$\|\eta\|$ (subl. τ)	1.77	1.76	0.99	0.98

The χ^2 values for the two-dimensional fake-factors show for the most part a slight improvement compared to the one-dimensional ones. Exceptions are the RNN-ID values in m_T^{tot}, where there is no significant difference. This is mostly in agreement with our expectations, since the difference in the curves for the fake-factor in the respective binnings of $|\eta|$ were also pretty slight. The improvements offered by binning the fake-factor in a second dimension of $|\eta|$ are probably not significant enough to warrant including it in future analyses regarding the modelling of m_T^{tot}, but a possible benefit in other applications, e.g. multivariate analysis, is not precluded.

7 Conclusion

In this Bachelor thesis, the ATLAS search for heavy neutral Higgs bosons in the $H/A \to \tau\tau$ channel [34] with a focus on the $\tau_{had}\tau_{had}$ final state was examined with the results for the M_h^{125} benchmark scenario, where parts of the $m_A - \tan\beta$ plane could be excluded at 95% CL. No significant deviation above from the SM background was observed in this analysis.
A possible improvement to the data-driven technique used in the estimation of the multijet background, the fake-factor method, was analyzed in this thesis. In the use of this method a second variable, on which the fake-factor depends, was introduced in addition to the already existing binning in the p_T of the subleading $\tau_{\text{had-vis}}$ candidate. The variable chosen was the $|\eta|$ of the subleading $\tau_{\text{had-vis}}$ candidate, since the fake-factor had the next-largest dependence on it. The background estimate was revisited with this two-dimensional dependence of the fake-factor for both the BDT τ lepton identification algorithm and the RNN one.
The results have shown that while there is a slight improvement of approximately 1% in the modelling of the multijet background estimate using the two-dimensional fake-factor, it does not make enough of a difference to include for the modelling of m_T^{tot}. Especially in the RNN-ID, with which the future search in the $H/A \to \tau\tau$ channel will be performed, the two-dimensional fake-factor has shown no real improvement over the standard one. Nonetheless, a possible application of the two-dimensional fake-factor might be multivariate analysis using the p_T or $|\eta|$ of the subleading $\tau_{\text{had-vis}}$ candidate, since even small improvements to the modelling might have significant benefits.
The next step in the analysis would be to include the systematic errors, which unfortunately in the case of the RNN-ID were not yet available at the time of this thesis. A future analysis might be able to further validate the value of the improvements brought forth by the two-dimensional fake-factor by including these errors.
The search for physics beyond the Standard Model continues. When the installation of the High Luminosity LHC [41] will be finished, there will be even more data to be analyzed regarding physics beyond the Standard Model due to the anticipated raise in the integrated luminosity, at an increased centre-of-mass energy of $\sqrt{s} = 14$ TeV. For higher energies, a new particle accelerator would need to be built. In any case, continuing to

push the boundaries of experimental research in hopes of understanding phenomena at ever higher energy scales will keep particle physicists occupied for probably quite some time.

A Additional Plots BDT-ID and RNN-ID

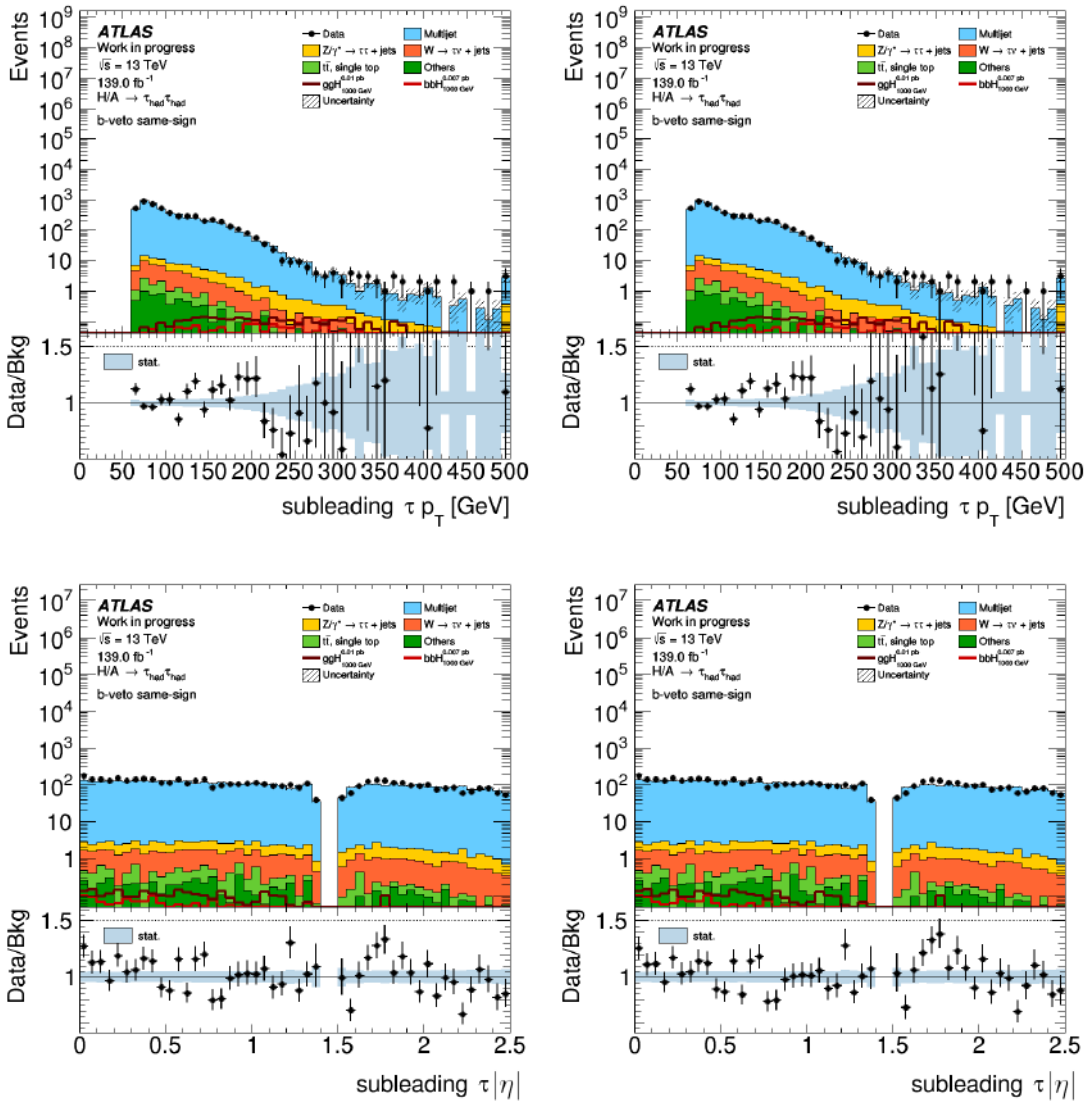

Figure A.1: Plots of $|\eta|$ (upper plots) and p_T (second row) of the subleading τ candidate in the validation region without binning of the fake factor in $|\eta|$ (left) and with (right) based on BDT τ-ID

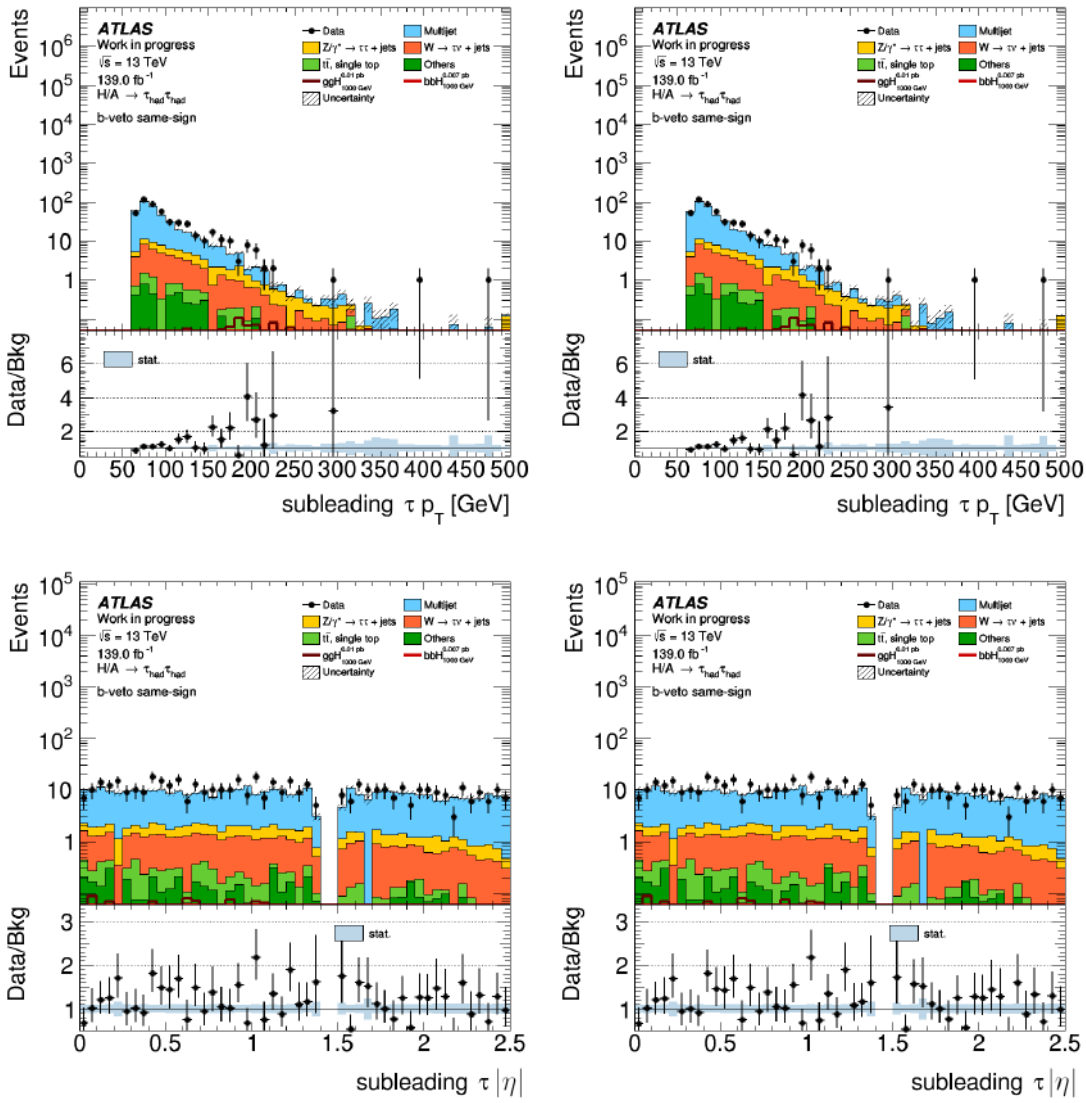

Figure A.2: Plots of $|\eta|$ (first row) and p_T (second row) of the subleading τ candidate and $\Delta\phi$ (third row) in the validation region without binning of the fake factor in $|\eta|$ (left) and with (right) based on RNN τ-ID

Bibliography

[1] M. K. Gaillard, P. D. Grannis, F. J. Sciulli, *The Standard model of particle physics*, Rev. Mod. Phys. **71**, S96 (1999)

[2] S. L. Glashow, *Partial-symmetries of weak interactions*, Nucl. Phys. **22(4)**, 579 (1961)

[3] *Standard Model of Particle Physics* (Accessed: 2020-08-20), URL `https://en.wikipedia.org/wiki/Standard_Model`

[4] M. Gell-Mann, *Symmetries of Baryons and Mesons*, Phys. Rev. **125**, 1067 (1962)

[5] G. Altarelli, *A QCD primer*, AIP Conf. Proc. **631(1)**, 70 (2002)

[6] A. B. Arbuzov, *Quantum Field Theory and the Electroweak Standard Model* pages 1–34 (2017), `arXiv:1801.05670[hep-ex]`

[7] S. F. Novaes, *Standard model: An Introduction*, in *Particles and fields. Proceedings, 10th Jorge Andre Swieca Summer School, Sao Paulo, Brazil, February 6-12, 1999*, pages 5–102 (1999)

[8] N. Cabibbo, *Unitary Symmetry and Leptonic Decays*, Phys. Rev. Lett. **10**, 531 (1963)

[9] J. Goldstone, A. Salam, S. Weinberg, *Broken Symmetries*, Phys. Rev. **127**, 965 (1962)

[10] S. L. Glashow, *Partial-symmetries of weak interactions*, Nuclear Physics **22(4)**, 579 (1961)

[11] F. Englert, R. Brout, *Broken Symmetry and the Mass of Gauge Vector Mesons*, Phys. Rev. Lett. **13**, 321 (1964)

[12] P. W. Higgs, *Broken Symmetries And The Masses Of Gauge Bosons*, Phys. Rev. Lett. **13**, 508 (1964)

[13] G. S. G. et al, *Global Conservation Laws and Massless Particles*, Phys. Rev. Lett. **13**, 585 (1964)

[14] M. Thomson, *Modern Particle Physics*, Cambridge University Press (2013)

[15] P. Kroupa et al., *Local-Group tests of dark-matter Concordance Cosmology: Towards a new paradigm for structure formation?*, Astron. Astrophys. **523**, A32 (2010)

[16] R. Barbieri, A. Strumia, *The 'LEP paradox'*, in *4th Rencontres du Vietnam: Physics at Extreme Energies (Particle Physics and Astrophysics)* (2000)

[17] V. Trimble, *Existence and Nature of Dark Matter in the Universe*, Annual Review of Astronomy and Astrophysics **25(1)**, 425 (1987)

[18] S. Dimopoulos, S. Raby, F. Wilczek, *Supersymmetry and the scale of unification*, Phys. Rev. D **24**, 1681 (1981)

[19] C. Csaki, *The Minimal supersymmetric standard model (MSSM)*, Mod. Phys. Lett. A **11**, 599 (1996)

[20] S. Dimopoulos, H. Georgi, *Softly Broken Supersymmetry and SU(5)*, Nucl. Phys. B **193**, 150 (1981)

[21] M. Carena, S. Heinemeyer, O. Stål, C. Wagner, G. Weiglein, *MSSM Higgs Boson Searches at the LHC: Benchmark Scenarios after the Discovery of a Higgs-like Particle*, Eur. Phys. J. C **73(9)**, 2552 (2013)

[22] A. Djouadi et al., *The post-Higgs MSSM scenario: Habemus MSSM?*, Eur. Phys. J. C **73**, 2650 (2013)

[23] E. Bagnaschi, et al., *MSSM Higgs Boson Searches at the LHC: Benchmark Scenarios for Run 2 and Beyond*, Eur. Phys. J. C **79(7)** (2019)

[24] ATLAS Collaboration, *Observation of a new particle in the search for the Standard Model Higgs boson with the ATLAS detector at the LHC*, Phys. Lett. B **716**, 1 (2012)

[25] ATLAS Collaboration, *Search for additional heavy neutral Higgs and gauge bosons in the ditau final state produced in 36 fb^{-1} of pp collisions at $\sqrt{s} = 13$ TeV with the ATLAS detector*, JHEP **01**, 055 (2018)

[26] L. Evans, P. Bryant, *LHC Machine*, JINST **3(08)**, S08001 (2008)

[27] *LHC acceleration chain* (Accessed: 2020-08-20), URL `https://cds.cern.ch/images/OPEN-PHO-ACCEL-2013-056-1`

[28] ATLAS Collaboration, *The ATLAS Experiment at the CERN Large Hadron Collider*, JINST **3**, S08003 (2008)

[29] *ATLAS Detector* (Accessed: 2020-08-20), URL `https://cds.cern.ch/record/1267853/files/atlas.png`

[30] *Illustration of the ATLAS coordinate system* (Accessed: 2020-08-20), URL `https://cds.cern.ch/record/1699952/files/Figures_T_Coordinate.png`

[31] *Inner Detector* (Accessed: 2020-08-20), URL `https://atlas.cern/discover/detector/inner-detector`

[32] ATLAS Collaboration, *The ATLAS Inner Detector commissioning and calibration*, Eur. Phys. J. C **70**, 787 (2010)

[33] ATLAS Collaboration (ATLAS), *Operation of the ATLAS trigger system in Run 2* (2020), `2007.12539`

[34] ATLAS Collaboration, *Search for heavy Higgs bosons decaying into two tau leptons with the ATLAS detector using pp collisions at* $\sqrt{s} = 13$ *TeV*, Phys. Rev. Lett. **125(5)** (2020)

[35] M. Cacciari, G. P. Salam, G. Soyez, *The anti-k_t jet clustering algorithm*, JHEP **04**, 063 (2008)

[36] ATLAS Collaboration, *ATLAS b-jet identification performance and efficiency measurement with $t\bar{t}$ events in pp collisions at* $\sqrt{s} = 13$ *TeV*, Eur. Phys. J. C **79(11)**, 970 (2019)

[37] K. Olive, *Review of Particle Physics*, Chinese Physics C **38(9)**, 090001 (2014)

[38] ATLAS Collaboration, *Reconstruction, Energy Calibration, and Identification of Hadronically Decaying Tau Leptons in the ATLAS Experiment for Run-2 of the LHC*, Technical Report ATL-PHYS-PUB-2015-045, CERN, Geneva (2015)

[39] ATLAS Collaboration, *Identification of hadronic tau lepton decays using neural networks in the ATLAS experiment*, Technical Report ATL-PHYS-PUB-2019-033, CERN, Geneva (2019)

[40] N. D. Gagunashvili, *Comparison of weighted and unweighted histograms* (2006), `arXiv:physics/0605123[physics.data-an]`

[41] G. Apollinari et al., *High-Luminosity Large Hadron Collider (HL-LHC): Technical Design Report V. 0.1*, CERN Yellow Reports: Monographs, Geneva (2017)

Acknowledgements

It is a truth universally acknowledged that Bachelor students are more trouble than they're worth, so I want to thank Lino for taking on the lion's share of this trouble. You never made me feel like I was asking a really stupid question, even when I really was. Also a heartfelt thank you to Stan, I think you would need to look far and wide to find a professor more dedicated to his students. The research chats every week helped us all stay on target.
Ein liebevolles Dankeschön an meine Familie und besonders Mama und Felix für eure Unterstützung in Allem!

Erklärung nach §13(9) der Prüfungsordnung für den Bachelor-Studiengang Physik und den Master-Studiengang Physik an der Universität Göttingen:
Hiermit erkläre ich, dass ich diese Abschlussarbeit selbständig verfasst habe, keine anderen als die angegebenen Quellen und Hilfsmittel benutzt habe und alle Stellen, die wörtlich oder sinngemäß aus veröffentlichten Schriften entnommen wurden, als solche kenntlich gemacht habe.
Darüberhinaus erkläre ich, dass diese Abschlussarbeit nicht, auch nicht auszugsweise, im Rahmen einer nichtbestandenen Prüfung an dieser oder einer anderen Hochschule eingereicht wurde.

Göttingen, den 8. November 2020

(Anne Gaa)